The Effect of Leading-Edge Geometry on the Induced Drag of a Finite Wing

by

Che Wei Ou

A Thesis Presented in Partial Fulfillment
of the Requirements for the Degree
Master of Science

Approved April 2019 by the
Graduate Supervisory Committee:

Timothy Takahashi, Chair
Huei-Ping Huang
Marcus Herrmann

ARIZONA STATE UNIVERSITY

May 2019

ABSTRACT

This study identifies the influence that leading-edge shape has on the aerodynamic characteristics of a wing using surface far-field and near-field analysis. It examines if a wake survey is the appropriate means for measuring profile drag and induced drag. The paper unveils the differences between sharp leading-edge and blunt leading-edge wings with the tools of pressure loop, chordwise pressure distribution, span load plots and with wake integral computations. The analysis was performed using Computational Fluid Dynamics (CFD), vortex lattice potential flow code (VORLAX), and a few wind-tunnels runs to acquire data for comparison. This study found that sharp leading-edge wings have less leading-edge suction and higher drag than blunt leading-edge wings.

The blunt leading-edge wings have less drag because the normal vector of the surface in the front section of the airfoil develops forces at opposed skin friction. The shape of the leading edge, in conjunction with the effect of viscosity, slightly alter the span load; both the magnitude of the lift and the transverse distribution. Another goal in this study is to verify the veracity of wake survey theory; the two different leading-edge shapes reveals the shortcoming of Mclean's equation which is only applicable to blunt leading-edge wings.

ACKNOWLEDGMENTS

This thesis is supported by Galen P. Kingsley's undergraduate project, Martin Morrow's Barrett Thesis experimental models, and supervised by Timothy T. Takahashi.

TABLE OF CONTENTS

Page

LIST OF TABLES v

LIST OF FIGURES vi

INTRODUCTION 1

PRIOR ART 3

A. Induced Drag Derivation 3

1. Drag Due to Lift from Downwash Only 3

2. Drag Due to Lift via Lifting Line Theory 5

3. Correctness of Ellipticality 14

4. Inviscid Drag from Wake Momentum Changes 16

5. Vortex Drag and Induced Drag due to Wake Momentum Changes 19

6. Induced Drag using Trefftz Planes 22

B. Induced Drag Derivation: Stream and Velocity Potential Functions 24

C. Induced Drag Derivation: From Lifting Line Theory to VLM 27

D. Proposed Induced Drag Corrections 30

1. Henderson's Leading-edge Suction Parameter 30

2. Polhamus: "Leading-edge Suction" Drag Coefficient Correlation 32

3. Pressure Loops and the Concept of Leading-edge Suction 39

4. Analytical Correction as applied to Vortex Lattice Calculations 42

Page

MODELS AND RAW DATA 46

A. Description of Wind Tunnel Test 46

B. Description of Flat Plate VORLAX Model 47

C. Description of Thick “Sandwich” VORLAX Model 51

D. Description of AUTODESK CFD Model 56

RESULT AND DISCUSSION 64

A. Verify CFD Results with Wind Tunnel Data and VORLAX Code 64

B. Utilize Pressure Loop to Observe the Leading-edge Suction. 67

C. Infer the Transverse Span Load to Extract the Classical Bound Vorticity Distribution 70

D. Chordwise Pressure Distribution 75

E. Mclean’s Equation Verification 78

CONCLUSION 90

REFERENCES 93

LIST OF TABLES

Table Page

Table 1: VORLAX Flat Panel Result 50

Table 2: Surface Ordinates Distribution for a NACA0012 Wing..... 52

Table 3: Surface Ordinates Distribution for a Biconvex Wing..... 54

Table 4: Turbulent Models Test..... 57

LIST OF FIGURES

Figure Page

Figure 1: Max Munk's Circular Downwash Influence Model[1] 3

Figure 2: Prandtl Lifting Line Theory[8] 6

Figure 3: Circulation around an airfoil 6

Figure 4: The Difference of Joukowski Transformation and Real Situation 7

Figure 5: Downwash Angle αi 8

Figure 6: The Derivation of Induced Drag does not Include Axial Forces or Thickness Effects. 10

Figure 7: The Pressure Forces are Point to a Center Point Instead of Normal to the Surface. 15

Figure 8: Bollay Definition of the Control Volume Needed to Express the Drag of a Lifting Surface[13] 17

Figure 9: The Concept of Trefftz Plane from Mclean's Book[3] 22

Figure 10: Concept of Lifting Surface Theory from "Fundamentals of Aerodynamics"[8] 29

Figure 11: Polhamus Perspective[26] 32

Figure 12: Neglect the Axial Force During the Derivation of Lift Coefficient. 33

Figure 13: Kp versus Aspect Ratio[26] 33

Figure 14: Relationship Between Cs and C_T from Polhamus's paper [26] 35

Figure 15: Variation of Kv with Aspect Ratio for Sharp-edge Delta Wings from Polhamus's Paper[26]. 37

Figure 16: Classical CP vs Chord Plot (from ARC R&M 60) 39

Figure Page

Figure 17: Suction Loop CP vs Z' Plot (from ARC R&M 60) 39

Figure 18: NACA 0012 and Biconvex Airfoil Coordinates 40

Figure 19: Comparison of Cosine and Sine Components for the Normal Vector of the Mesh Panels Between a NACA 0012 Airfoil and a Biconvex Airfoil. 41

Figure 20: Direction Cosines NACA 0012 Airfoil at 5-degree Angle of Attack. 42

Figure 21: Geometry Stretching of Prandtl-Glauert Transformation(from Jones's Book[30]) 43

Figure 22: Two Approaches to Calculate Sideslip Effect 44

Figure 23: Leading-Edge Suction Correction 45

Figure 24: NACA0015: CL versus α 46

Figure 25: NACA0015: CD versus α 46

Figure 26: Drag Polar with Experimental Data 47

Figure 27: Panels Lattice for Thin Plate Model and Sandwich Model[4] 47

Figure 28: Full Leading-edge Setup for an Aspect Ratio 3 Airfoil. 48

Figure 29: No Leading-edge Setup for an Aspect Ratio 3 Airfoil. 49

Figure 30: Leading-edge Suction Comparison 50

Figure 31: VORLAX Drag Polar Comparison 51

Figure 32: Surface Ordinates Distribution for a NACA0012 Wing 53

Figure 33: Surface Ordinates for a Biconvex Wing. 55

Figure 34: Geometry Setup 58

Figure 35: Mesh Around the Airfoil 58

Figure 36: Wireframe for Control Volume 58

Figure Page

Figure 37: Wall Layers 59

Figure 38: Convergence Plot (Residual) 60

Figure 39: Convergence Plot (DPhi/Phi) 60

Figure 40: Convergence Plot (Average) 61

Figure 41: Velocity Field for a NACA0012 Airfoil from Zero to Eight Angle of Attack 62

Figure 42: Velocity Field for a Biconvex Airfoil from Zero to Eight Angle of Attack. .. 62

Figure 43: Pressure Field for a NACA0012 Airfoil from Zero to Eight Angle of Attack 62

Figure 44: Pressure Field for a Biconvex Airfoil from Zero to Eight Angle of Attack.... 63

Figure 45: Lift Coefficient versus Angle of Attack 64

Figure 46: Drag Polar..... 66

Figure 47: Pressure Loops for NACA 0012 Airfoil from 1° to 8° angle-of-attack 67

Figure 48: Pressure Loops for Biconvex Airfoil from One to Eight Angle-of-Attack..... 69

Figure 49: Normal Vector for the Middle Point of Each Panel. 70

Figure 50: Comparison of Cosine and Sine Components for the Normal Cector of the Mesh Panels Between a NACA 0012 Airfoil and a Biconvex Airfoil. 71

Figure 51: Span Loads for a NACA0012 Airfoil from One to Eight Angle of Attack..... 73

Figure 52: Span Loads for a Biconvex Airfoil from One to Eight Angle of Attack. 74

Figure 53: Pressure Distribution for a NACA 0012 Airfoil 76

Figure 54: Pressure Distribution for a Biconvex 0012 Airfoil 77

Figure 55: Wake Survey Plane and Induced Drag for a NACA0012 Airfoil from Mclean's Equation 78

Figure Page

Figure 56: Wake Survey Plane and Induced Drag for a Biconvex Airfoil from Mclean's Equation 79

Figure 57: Post-processing for VORLAX Wake Integration (Blunt leading-edge) 80

Figure 58: Post-processing for VORLAX Wake Integration (Sharp leading-edge)..... 80

Figure 59: Mclean's Wake Integral for Blunt Leading-edge..... 82

Figure 60: Mclean's Wake Integral for Sharp Leading-edge 83

Figure 61: Velocity Flow Across a Biconvex Airfoil..... 84

Figure 62: The Vortex Behind a Biconvex Airfoil 84

Figure 63: The Pressure Loop for a Biconvex Wing at 8° angle-of-attack. (CFD only).. 85

Figure 64: The Pressure Loop for a NACA0012 Wing at 8° angle-of-attack. (Both CFD and VORLAX)..... 86

Figure 65: Pressure Force Distribution. [37] 87

INTRODUCTION

"Induced drag is an evil, because all drag is an evil, but it is a necessary evil at least and expended for something we want," says Max M. Munk[1]. There are many sources of drag, but induced drag is the most inevitable one for generating lift. In classical aerodynamics, induced drag increases with the square of the lift. Traditional methods to reduce induced drag include increasing the aspect ratio, adding a winglet, or making the span load more elliptical. The most famous example is the Supermarine Spitfire in World War II which had an elliptical planform wing. However, elliptical planform wings have a complicated structure and also other studies show that this planform doesn't inherently develop an elliptical span load[2]. Hence, wingtip and tapered wing are the main resorts in modern aviation.

The formation of induced drag comes from downwash flow generated by deflection of airflow. The downwash flow reduces relative incoming flow thereby decreases the effective angle of attack to create lift. The classical theory developed by Max M. Munk[1] elaborates on the meaning of induced drag as a reaction force of lift worked on the air. In the other hand, Mclean[3] defines induced drag as a measure of energy loss and calculates the induced drag from the disturbance of wake flow.

This thesis aims to verify the previous theories made by famous aerodynamic researchers and discusses the influence of leading-edge geometry on induced drag, to understand induced drag from different perspective. It uses the vortex lattice method

potential flow solutions[4] and Computational Fluid Dynamics (CFD)[5] to provide the essential data for an inviscid model and a viscid model.

The primary objective of the thesis is to determine the relationships of leading-edge geometry and use a proper correction factor to correlate the theory with the phenomena.

PRIOR ART

A. Induced Drag Derivation

The derivation of induced drag is often determined from the perspective of lift developed by “bound vortices” generated across the span. Two different paths of reasoning are considered in the study: drag as derived from lift due to downwash and drag as derived from lift from Prandtl’s lifting line theory.

1. Drag Due to Lift from Downwash Only

Max Munk proposed[1] that a lifting wing generates lift because the air flow is deflected by the wing. The lift can be calculated as the change in momentum due to the downwash velocity. In his statement, the downwash area affected by wings must be the same as the span of the wings. The air flowing through the shaded area is shown in Figure 1:

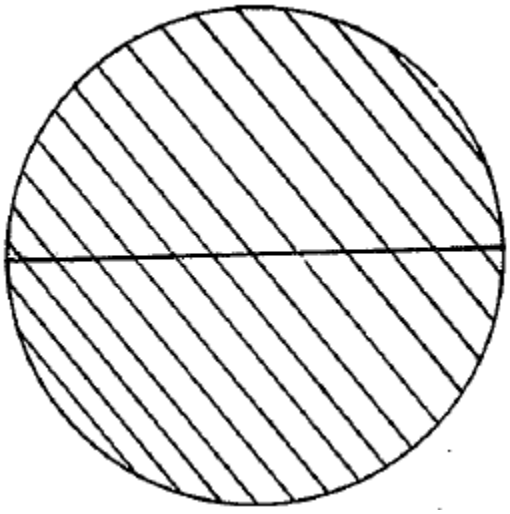

Figure 1: Max Munk's Circular Downwash Influence Model[1]

$$L = \dot{m} V_d \tag{1}$$

Where V_d is the downwash velocity and $\dot{m}$ is the mass flow rate through the circular area shown below as:

$$\dot{m} = \frac{1}{4} \pi b^2 V_\infty \rho \tag{2}$$

Where b is the wing span, V_∞ is the freestream velocity, and ρ is the air density.

Why is the area of influence the shaded cylinder? It seems to be Pohlhausen's idea[6][7], but an extensive literature search hasn't found a rigorous derivation.

From here, it is determined that the kinetic energy through this region can simply be defined as:

$$KE_d = \frac{1}{2} \dot{m} V_d^2 = \frac{1}{2} * \frac{L^2}{\dot{m}} = \frac{L^2}{\frac{1}{2} \pi b^2 V_\infty \rho} \tag{3}$$

Following the work-energy theorem, drag can be defined in terms of the kinetic energy changes in the "wake" flow behind the wing.

$$D_i = \frac{KE_d}{V_\infty} = \frac{L^2}{\pi b^2 q_\infty} \tag{4}$$

where $q_\infty = \frac{1}{2} \rho V_\infty^2$ is the incompressible freestream dynamic pressure.

To convert these forces into coefficient form, we use the following relationship between b^2 and S_{ref}:

$$b^2 = S_{ref} * AR \tag{5}$$

where AR is the aspect ratio of the wing. Substituting this into Equation (4)

$$D_i = \frac{KE_d}{V_\infty} = \frac{L^2}{\pi b^2 q_\infty} \tag{4}$$

, and dividing both sides by $q * S_{ref}$, we can determine the induce drag coefficient:

$$\frac{D_i}{q * S_{ref}} = \frac{L^2}{\pi * AR * (q * s_{ref})^2} \tag{6}$$

$$C_{D_i} = \frac{C_L^2}{\pi * AR} \tag{7}$$

Note that Munk's method does not accurately calculate the induced drag for non-elliptical loadings. In addition, his method does not consider the effect of the nuanced thickness or camber of the wing in this purely ideal flow-field based estimation of induced drag will show later that Munk's method (the Pohlhausen cylinder of downwash) seems contrived to fit experimental data for blunt leading-edge wings with elliptical transverse span loads.

2. Drag Due to Lift via Lifting Line Theory

Anderson [8], as well as Bertin & Cummings [9], also derive induced drag from the downwash velocity field, but in the context of Prandtl's lifting line theory [10]. Prandtl, in turn, determines lift from the circulation of the spanwise vortices shown in Figure 2.

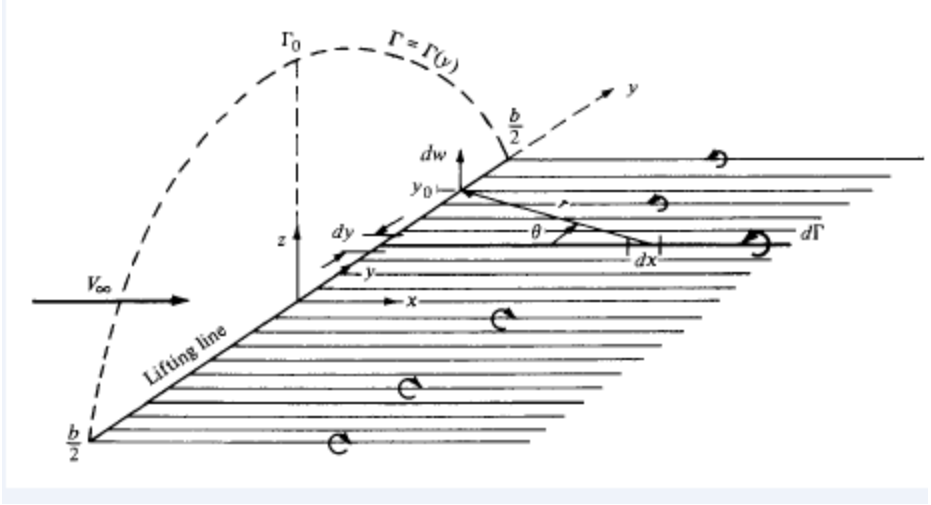

Figure 2: Prandtl Lifting Line Theory[8]

Given there is a limitation with the circulation defined along the span, with the range of $-\frac{b}{2}$ to $+\frac{b}{2}$, each spanwise component of lift is defined via the Kutta-Joukowski theorem:

$$L'^{(y_0)} = \rho_\infty V_\infty \Gamma(y_0) \tag{8}$$

Where Γ is the circulation (see Figure 3) and y_0 is a specific transverse "strip" on the span.

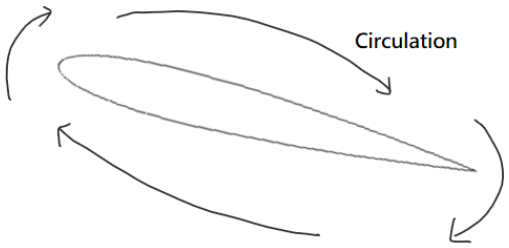

Figure 3: Circulation around an airfoil

Observe that Kutta-Joukowski theorem is composed of Kutta condition and Joukowski transformation. From Joukowski transformation [11], a circle can be mapped to

airfoil-like shape with a round leading-edge and a sharp trailing edge. From Kutta condition [12], the theorem can be applied to "sharp" trailing edge. Therefore, Kutta-Joukowski theorem does not consider the thickness or camber effect because the force acting on the surface are assumed to point to the center of the airfoil instead of normal to the surface. (see Figure 4) Also, the theorem can only be applied to blunt leading-edge airfoil because of the Joukowski transformation.

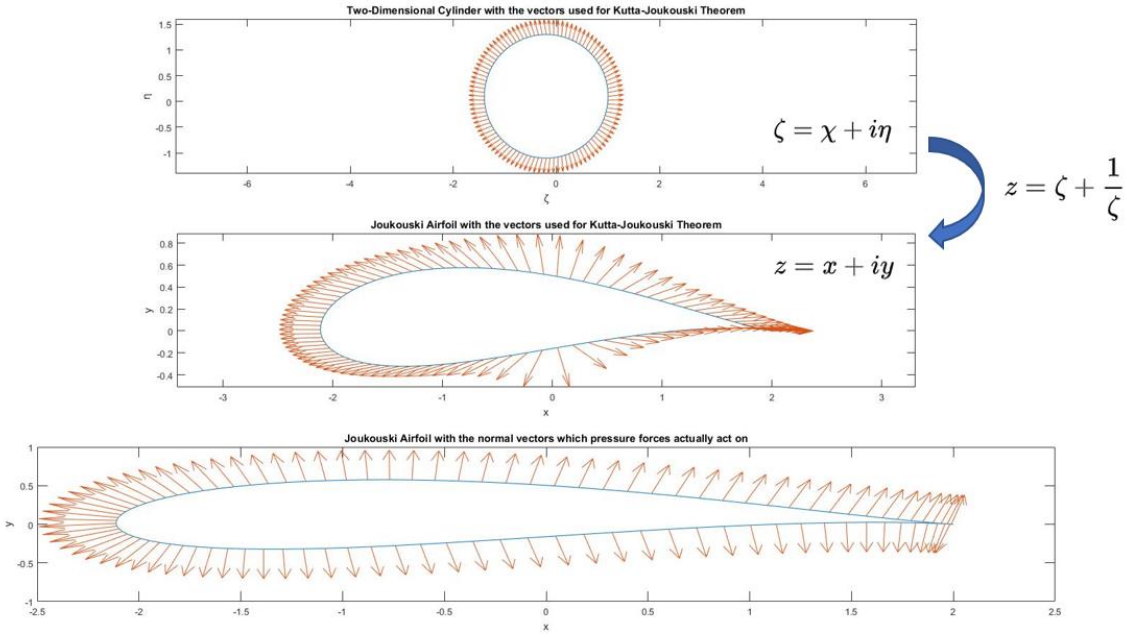

Figure 4: The Difference of Joukowski Transformation and Real Situation

Going back to the derivation of Lifting Line Theory, the classical theory[10] states that the total lift is simply an integration of the spanwise lift function:

$$L = \int_{-\frac{b}{2}}^{\frac{b}{2}} L'(y)dy = \rho_\infty V_\infty \int_{-\frac{b}{2}}^{\frac{b}{2}} \Gamma(y)dy \tag{9}$$

Or, in coefficient form:

$$C_L = \frac{2}{V_\infty S_{ref}} \int_{-\frac{b}{2}}^{\frac{b}{2}} \Gamma(y) dy \tag{10}$$

Due to the downwash velocity V_d not being parallel with the freestream velocity V_∞ , there is an induced angle of attack; for small angles where $tan\,\alpha \approx \alpha$ (in radians), the induced angle of attack can be defined as follows:

$$\alpha_i(y_0) = \frac{-V_d(y_0)}{V_\infty} \tag{11}$$

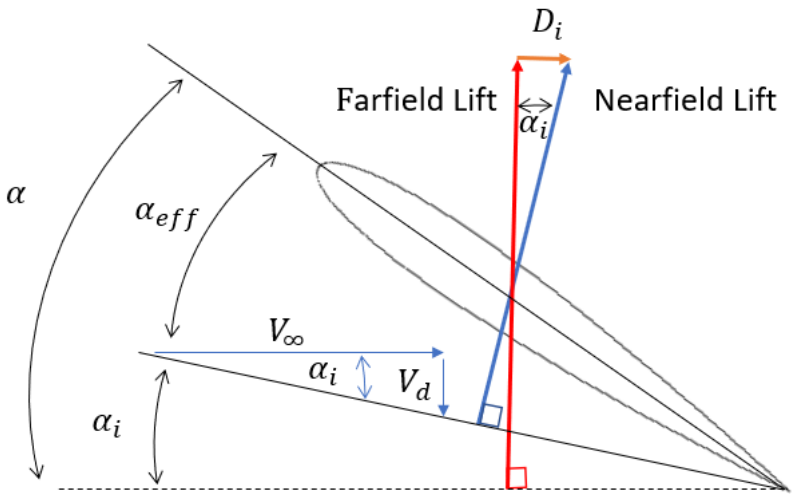

Figure 5: Downwash Angle α_i

Notice that Far-field Lift is what we calculate about, and near-field lift is a way to simplify two-dimensional airfoil theory to "work" in the consist of a finite wing. Moreover, the induced drag D_i in Figure 5 neglects any viscous or inviscid contribution from axial forces in two-dimension.

Below, the definition of downwash velocity is defined as the effect of all vortices on a single point on the span:

$$V_d(y_0) = -\frac{1}{4\pi}\int_{-\frac{b}{2}}^{\frac{b}{2}} \frac{1}{y_0 - y}\frac{d\Gamma}{dy}dy \tag{12}$$

Which is substituted into Equation (11) to calculate induced angle of attack purely based on freestream velocity and circulation:

$$\alpha_i(y_0) = \frac{1}{4\pi V_\infty}\int_{-\frac{b}{2}}^{\frac{b}{2}} \frac{1}{y_0 - y}\frac{d\Gamma}{dy}dy \tag{13}$$

The drag due to lift at each spanwise point can then be calculated as the streamwise component of the normal force vector at this induced angle of attack, which again is assumed to be negligible so $sin\,\alpha_i = \alpha_i$:

$$D_i'(y_0) = L'\,sin\,\alpha_i(y_0) = L'\alpha_i \tag{14}$$

Where the thickness is neglected in the equation, and all angle of surface panels are perpendicular to radius direction. Beware, the source of the induced drag is only from purely rotation of flat plate lift, this treats all the normal vector of the surface is perpendicular to the chord, see Figure 6.

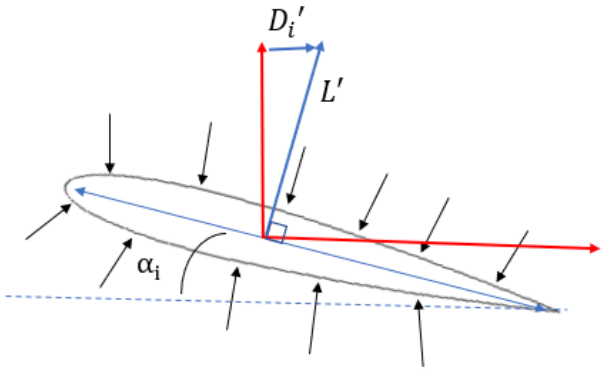

Figure 6: The Derivation of Induced Drag does not Include Axial Forces or Thickness Effects.

Substituting the spanwise lift from Equation (14) and following the same mathematical logic of integration across the span results in the following equation:

$$D_i = \rho_\infty V_\infty \int_{-\frac{b}{2}}^{\frac{b}{2}} \Gamma(y)\alpha_i(y)dy \tag{15}$$

Which in coefficient form becomes:

$$C_{D_i} = \frac{2}{V_\infty S_{ref}} \int_{-\frac{b}{2}}^{\frac{b}{2}} \Gamma(y)\alpha_i(y)dy \tag{16}$$

If we assume that the lift distribution is "elliptical," we may define the circulation as follows:

$$\Gamma(y) = \Gamma_0 \sqrt{1 - \left(\frac{2y}{b}\right)^2} \tag{17}$$

Where Γ_0 is the circulation at the origin. By substituting Equation (17) into Equation (16), and integrating the circulation along θ where $-\frac{b}{2} \leq y, = \frac{b}{2}$ is equivalent to $0 \leq \theta \leq \pi$, the

downwash can be calculated as a constant across the span which in turn results in the need for a constant induced angle of attack:

$$V_d(\theta_0) = -\frac{\Gamma_0}{2b} \tag{18}$$

$$\alpha_i = \frac{\Gamma_0}{2bV_\infty} \tag{19}$$

The value of the circulation at the origin is derived from the lift equation, where again the circulation is integrated across the transformed θ coordinates:

$$L = \frac{\rho_\infty V_\infty \Gamma_0 b}{4}\pi \tag{20}$$

$$\Gamma_0 = \frac{4L}{\rho_\infty V_\infty b\pi} = \frac{2V_\infty S_{ref} C_L}{b\pi} \tag{21}$$

Where, once again, the thickness is neglected.

By substituting the coefficient form of Equation (21) into Equation (19), the induced angle of attack becomes the following form:

$$\alpha_i = \frac{S_{ref} C_L}{\pi b^2} = \frac{C_L}{\pi AR} \tag{22}$$

With α_i constant, the integration for induced drag is simplified to the same form as calculated for lift, with Equation (22) substituted in coefficient form:

$$C_{D_i} = \frac{\pi \alpha_i \Gamma_0 b}{2V_\infty S_{ref}} = \frac{\pi b}{2V_\infty S_{ref}}\left(\frac{C_L}{\pi AR}\right)\left(\frac{2V_\infty S_{ref} C_L}{b\pi}\right) \tag{23}$$

$$C_{D_i} = \frac{C_L^2}{\pi AR} \tag{24}$$

Equation (24) is identical to the formula of induced drag assuming an elliptical lift distribution as derived by Munk. In a general form, not assuming an elliptical lift distribution, the circulation can be defined in the following form:

$$\Gamma(\theta) = \Gamma_0 \sin\theta = \frac{2V_\infty S_{ref} C_L}{b\pi} sin(\theta) \tag{25}$$

Given that the span is defined as the range $0 \leq \theta \leq \pi$ as performed in the previous derivation, the circulation can then be expanded to be represented by a Fourier sine series:

$$\Gamma(\theta) = 2bV_\infty \sum_{1}^{N} A_n \sin n\theta \tag{26}$$

Substituting this form of circulation results in the following lift coefficient and induced angle of attack equations in θ coordinates:

$$C_L = \frac{2b^2}{S_{ref}} \sum_{1}^{N} A_n \int_0^\pi \sin n\theta \sin\theta \, d\theta \tag{27}$$

$$\alpha_i(\theta) = \sum_{n=1}^{N} nA_n \frac{\sin n\theta}{\sin\theta} \tag{28}$$

The integral in the lift equation is only defined when $n = 1$, and therefore can be solved to determine the Fourier coefficient A_1:

$$C_L = \frac{A_1 \pi b^2}{S_{ref}} = A_1 \pi AR$$

$$A_1 = \frac{C_L}{\pi AR} \tag{29 - 30}$$

Solving for C_{D_i} by substituting Eqs. (30) and (29) into Equation (24) results in a Messier function:

$$C_{D_i} = \frac{2b^2}{S_{ref}} \int_0^{\pi} \left(\sum_{n=1}^{N} A_n \sin n\theta \right) \left(\sum_{n=1}^{N} A_n \sin n\theta \right) d\theta \tag{31}$$

However, this integral resolves to 0 in all cases except when the two Fourier series have the same n, where it converts to $\frac{\pi}{2}$; this allows for the following simplification:

$$C_{D_i} = \frac{2b^2}{S_{ref}} \left(\sum_{n=1}^{N} n A_n^2 \right) \frac{\pi}{2} = \pi AR \sum_{n=1}^{N} n A_n^2 = \pi AR * A_1^2 \left(1 + \sum_{n=1}^{N} n \left(\frac{A_n}{A_1} \right)^2 \right) \tag{32}$$

Which is purely the "drag" due to the rotation of the normal force vector.

If we define $\delta = \sum_1^N n \left(\frac{A_n}{A_1} \right)^2$ and substitute in A_1 into Equation (32), the following form for induced drag is produced:

$$C_{D_i} = \frac{C_L^2}{\pi AR} (1 + \delta) \tag{33}$$

Where then we classically define $e = \frac{1}{1+\delta}$, resulting in the familiar general form for induced drag:

$$C_{D_i} = \frac{C_L^2}{\pi AR * e} \tag{34}$$

By definition, $\delta \geq 0$, so $e \leq 1$, where a value of $e = 1$ would indicate an elliptical lift distribution.

3. Correctness of Ellipticality

In Equation (34), the elliptical lift distribution (e = 1) produces the minimum induced drag according to the lift, hence the situation is called “ideal.” Based on the Lifting Line Theory, the “ideal” condition, which is elliptical lift distribution, can be reached by an elliptical planform. However, the discussion by Dulin & Takahashi shows an elliptical planform might not perfectly match the elliptical lift distribution even in the absence of fuselage[2].

The implication of the equation is intriguing: it would seem that the drag produced by a non-elliptical lift distribution would still be proportional to C_L^2, albeit scaled up by a factor related to the “ellipticality” (or lack thereof) of the spanwise distribution. Back to the foundation of the theory, we must note that this theory considers a world where the induced drag is solely a function of the circulation distribution. It neglects any contributions to drag arising from the nuanced thickness or camber profile of the wing. Therefore, the equation can only for making an approximation to explain the relationship between induced drag coefficient and lift coefficient.

In Figure 7, the actual force is acting normal to the surface, but the Equation (34) is derived from Kutta-Joukowski theorem, which means the equation is based on a two-dimensional cylinder. The equation will neglect the thickness effect, so all circulation will be contributed to only lift, which the pressure forces can be seen that they only act to a center point.

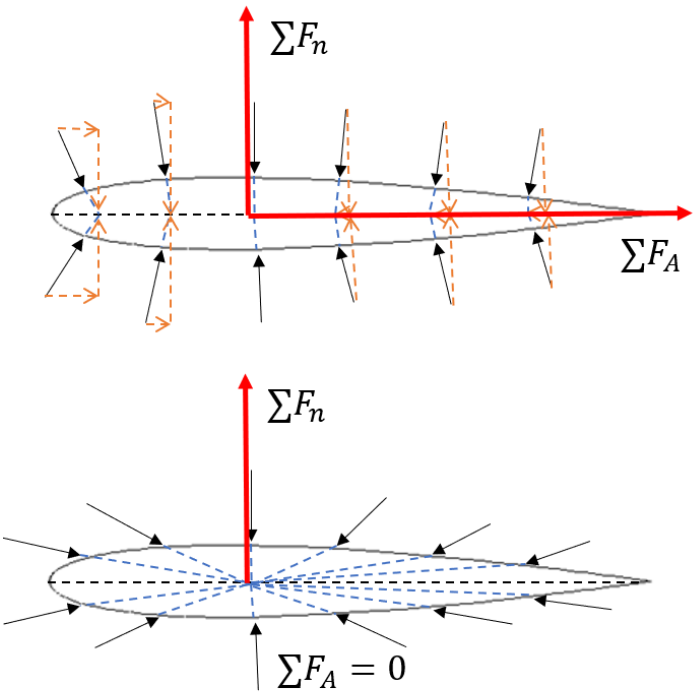

Figure 7: The Pressure Forces are Point to a Center Point Instead of Normal to the Surface.

The sketch shows real wings will develop an axial force $\sum F_A$ from an interaction between the pressure field and the airfoil shape. The Joukowski transformation can't present this feature in a real situation. Hence, the concept of "ellipticality" can only present an approximation to explain the real world.

4. Inviscid Drag from Wake Momentum Changes

Various authors have attempted to describe inviscid and induced drag effects via changes in momentum through a control volume, encapsulating the velocity changes in the wake of a wing[13]. Note the usage of the separate wording of "inviscid" and "induced": in some circles, the term "inviscid drag" has been equated with "induced drag," but in prior context of this paper the term "induced drag" has been used interchangeably with "drag-due-to-lift"; to maintain consistency, that equivalency will be maintained and the term "inviscid drag" will be used separately.

In 1997, Takahashi [13] compiled and examined a variety of momentum-based drag decomposition techniques. These methods are largely agnostic to lifting line theory; as such, they might allow for contributions to drag arising from the nuanced thickness and camber profile of the wing as well as contributions due to viscosity (skin friction) and flow separation.

Takahashi noted that Bollay [14] who sought to differentiate between inviscid drag effects and viscous boundary layer effects referred to as "profile drag." In the most general case, Bollay defines "profile drag" as the momentum losses due to change in static pressure and in axial momentum changes through a control volume; reference Figure 8:

$$D = \iint_{S_0} p_0 dS_0 + \iint_{S_0} \rho u_0^2 dS_0 - \iint_{S_1} p_1 dS_1 - \iint_{S_1} \rho u_1^2 dS_1 - \iint_{S_r} \rho u_t u_r dS_r \qquad (35)$$

Where S_0 is the upstream planar surface in front of the wing, S_1 is the downstream planar surface behind the wing, and S_r is the surface orthogonal to both upstream and downstream surfaces.

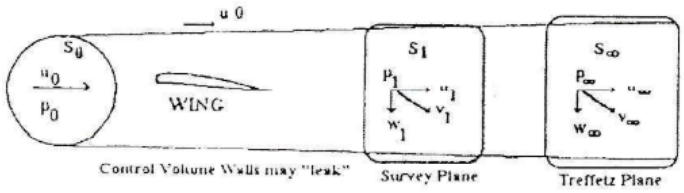

Figure 8: Bollay Definition of the Control Volume Needed to Express the Drag of a Lifting Surface[13]

Assuming that the surface S_r is far enough away from the body that the velocity $u_t = u_0$, then the mass flux will be zero across S_r and the momentum equation is as follows for inviscid drag:

$$D_i = \iint_{S_0} p_0 dS_0 + \iint_{S_0} \rho u_0^2 dS_0 - \iint_{S_1} p_{1_i} dS_1 - \iint_{S_1} \rho u_{1_i}^2 dS_1$$
$$= \iint_{S_0} (p_0 + \rho u_0^2) dS_0 + \iint_{S_1} (p_{1_i} + \rho u_{1_i}^2) dS_1 \quad (36)$$

Note the specific usage of p_{1_i} and u_{1_i} and the pressure and velocity respectively at the downstream plane due purely to inviscid losses, as opposed to the total pressure and velocity losses. Introducing Bernoulli's incompressible equation in 3D:

$$h = p + \frac{1}{2}\rho(u^2 + v^2 + w^2) \quad (37)$$

Where h is the total pressure, and u, v, and w are the x, y, and z components of velocity respectively. We can hereby assume that the upstream velocity is uniform with no vorticity, which means the combination of Equation (37) and (36) results in the following:

$$D_i = \iint_{S_0} \left(h_0 + \frac{1}{2}\rho u_0^2\right) dS_0 - \iint_{S_1} \left[h_{1_i} + \frac{1}{2}\rho\left(u_{1_i}^2 - v_{1_i}^2 - w_{1_i}^2\right)\right] dS_1 \qquad (38)$$

Combining and algebraically manipulating Equation (38) and (36) together results in the final form of inviscid drag as investigated by Bollay:

$$D_i = \iint_{S_1} \left[\frac{1}{2}\rho\left(v_{1_i}^2 + w_{1_i}^2\right)\right] dS_1 + \iint_{S_1} \left[\frac{1}{2}\rho\left(u_0^2 - u_{1_i}^2\right)\right] dS_1 \qquad (39)$$

The first integral, containing only non-axial velocity terms, represents the loss of cross-plane kinetic energy due to generated vortices. The second integral accounts for the inviscid losses in axial kinetic energy. This makes for an interesting perspective on inviscid drag: it accounts for drag purely from an energy perspective, as Munk's approach did; it is applicable to general lift distribution cases. These methods effectively account for downwash through the non-axial velocity terms without introducing any explicit circulation term.

While not being explicitly drag-due-to-lift, Equation (39) still explains at some level the drag losses due to sources outside of viscous boundary layer effects, which are accounted for separately in what is defined as "profile drag."

However, as mathematically graceful as this is, there is a considerable challenge to individually determine inviscid velocity changes from an experimental perspective.

On the bright side, we can use inviscid as well as viscous CFD solutions to explore the meaning of these equations.

5. Vortex Drag and Induced Drag due to Wake Momentum Changes

Betz [15] also decomposes drag into induced drag and profile drag similar to Bollay [14], though induced drag is defined as drag-due-to-lift and profile drag is defined as drag-not-due-to-lift. Betz attempts to calculate profile drag on its own, outside of defining the profile drag simply as the difference between total drag and induced drag. The control volume is similarly defined with upstream and downstream planes and an orthogonal plane with no mass flux through its surface, making the total drag equation considering one-dimensional total pressure as follows:

$$D = \iint_{S_0} (h_0 + \rho u_0^2) dS_0 - \iint_{S_1} (h_1 + \rho u_1^2) dS_1 \tag{40}$$

Betz identifies the difficulty of working with this equation as being due to the discontinuity of the integral across the downstream surface; that is, velocity changes locally based on generated vortices. Therefore, he introduces an additional velocity term, u', which he defines as being equivalent to u_1 outside of the region affected by the vortices. From a potential flow perspective, the additional velocity term is accounted for by introducing a source in the control volume, defined as having the following yield:

$$E = \iint_{S_1} (u' - u_1) dS_1 \tag{41}$$

What makes this equation particularly interesting is his following discussion of drag generated by the momentum change in the vortices. If no lift is generated, the drag generated is due to the source and is negative:

$$D' = -\rho u_0 E = \iint_{S_1} \frac{1}{2}\rho\left(u_0^2 - u'^2\right) dS_1 \tag{42}$$

In a case with lift, the induced drag is considered by Betz to be purely due to the downward component of velocity, w, which Betz equates to downwash:

$$D_i = \iint_{S_1} \frac{1}{2}\rho w^2 dS_1 \tag{43}$$

The total vortex drag is then considered to be the algebraic sum of the induced drag and the zero-lift vortex drag case:

$$D' = D_i - \rho u_0 E = \iint_{S_1} \frac{1}{2}\rho\left(u_0^2 - u'^2 + w^2\right) dS_1 \tag{44}$$

The equation makes for a rather intriguing idea: the drag generated by the vortices from the wing is not only due to the downward component of velocity, but also must account for the axial velocity change in the wake.

In Betz's original papers, he limits himself to consider two-dimensional flow (he neglects spanwise flow, which Takahashi [13] and Bollay [14] considered in their extensions of Betz).

McLean [3] also proposes a simple form of induced drag based on wake momentum changes. Assuming steady, inviscid flow, the mass flux can be stated simply as the double integral of the u velocity change across the downstream surface S_1:

$$\dot{m} = \iint_{S_1} \rho(u_0 - u_{1_i}) dS_1 \tag{45}$$

As before u_{1_i} indicates an inviscid assumption for the wake condition. The simple momentum equation for a purely inviscid case such as the one below is assumed to be induced drag (further confusing the boundary between inviscid drag and drag-due-to-lift):

$$D_i = \iint_{S_1} (p_{1_i} - p_0) dS_1 - \iint_{S_1} \rho(2u_0 u_{1_i} + u_{1_i}^2) dS_1 - \dot{m} u_0 \tag{46}$$

Applying Bernoulli's equation in three dimensions to express the pressure terms in the velocity components, with the same assumption that the upstream condition only consists of axial flow, the "induced drag" then reduces to the following equation:

$$\mathrm{D_i} = \iint_{\mathrm{S_1}} \frac{1}{2} \rho(-\mathrm{u_{1_i}^2} + \mathrm{v_{1_i}^2} + \mathrm{w_{1_i}^2}) \mathrm{dS_1} \tag{47}$$

Equation (47) presents an incredibly graceful form for determining induced drag. However, as with Bollay's equation, measuring the velocities due to inviscid changes alone is not a trivial challenge.

6. Induced Drag using Trefftz Planes

An alternative method for defining the control volume consists of determining the downstream plane S_1 infinitely far downstream, known as a Trefftz plane. (Figure 9)

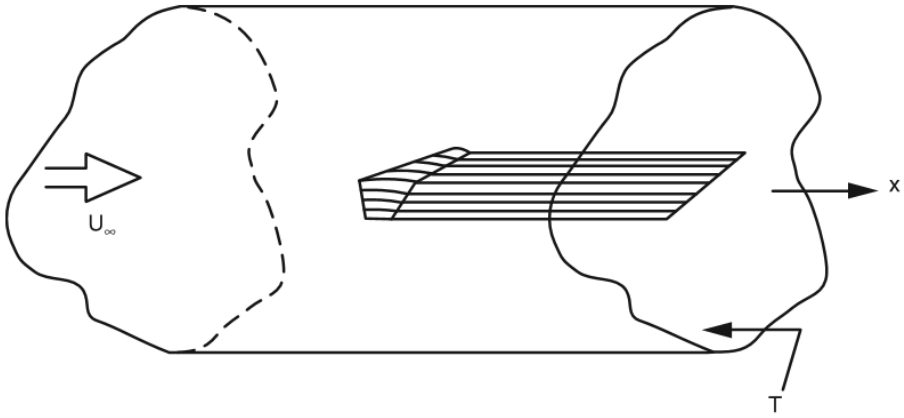

Figure 9: The Concept of Trefftz Plane from Mclean's Book[3]

McLean [3] notes that Trefftz plane methods assume a vortex sheet that does not "roll up" on the sides, which is then defined as a stream surface with no force acting on it. However, assuming that the vortices act along filaments as they propagate from the wing (per the Kutta-Joukowski theorem) there must be some force orthogonal to both velocity and vorticity vectors, which would be simply lift and induced drag.

From the Biot-Savart Law, McLean notes that the following equation is one way of expressing induced drag:

$$D_i = \frac{1}{2}\rho \int v_n \Gamma(l) dl \tag{48}$$

where the integral is along the line of the vortex sheet intersecting with the Trefftz plane, v_n is the magnitude of the velocity vector perpendicular to the line, and $\Gamma(l)$ is the circulation at each point along the vortex sheet.

Since the trailing vortices are the only wakes included into the integration and the distribution of vortex strength depends only on the spanwise distribution of lift and on the shapes of the lifting surfaces in the rear view called "Trefftz-plane view"[3], the result can be referenced back to the Munk's equation:

$$C_i = \frac{C_L^2}{\pi AR} \tag{7}$$

This method, as McLean points out, is mathematically sound but physically unintuitive, and in this form is typically used with values calculated from CFD. Moreover, we need to remember that the derivations are based on Lifting-Line Theory which the thickness effect is neglected.

Takahashi [13] outlined another Trefftz plane method by B. M. Jones[16] that uses a more readily applicable form of induced drag. Given a Trefftz plane where thus $p_0 = p_\infty$, the incompressible momentum equation is defined as follows:

$$D_i = \iint_{S_1} \rho * u_1(u_0 - u_\infty) dS_1 \tag{49}$$

If the total kinetic energy in the wake remains constant as Jones postulates, then the incompressible velocities can all be defined as follows:

$$u_\infty = \sqrt{\frac{2}{\rho}(h_1 - p_0)} \tag{50}$$

$$u_0 = \sqrt{\frac{2}{\rho}(h_0 - p_0)} \tag{51}$$

$$u_1 = \sqrt{\frac{2}{\rho}(h_1 - p_1)} \tag{52}$$

This then allows the incompressible momentum equation to be rewritten as follows:

$$D_i = 2\iint_{S_1} \left[\sqrt{h_1 - p_1} * \left(\sqrt{h_0 - p_0} - \sqrt{h_1 - p_0}\right)\right] dS_1 \tag{53}$$

Note that this form of "induced drag" proves to be experimentally convenient in that it is only dependent on the readily-measurable total and static pressures, though it is mathematically cumbersome to integrate. Another thing is that the method captures the thickness effects that manifest themselves in the downstream flow at the Trefftz planes.

B. Induced Drag Derivation: Stream and Velocity Potential Functions

The reader should note that these theories consider a world where the induced drag is solely a function of the stream function and potential distribution. They neglect any contributions to "induced drag" arising from the nuanced thickness or camber profile of the wing.

In 1972, Maskell [10][11] performed a method to decompose the induced drag and viscous drag and presented them by velocity potential function and stream function in three-dimensional space. The theory has been widely used in many well-known papers and books.

Takahashi notes [13] that Maskell defines Betz's two-dimensional formula as the profile drag and combine with the induced drag term.

$$\mathrm{D} = \int\int [(P_\infty - P) + \frac{\rho}{2}(u^* - u)\big(u^* + u - 2(U_\infty + u_b)\big)dS + \frac{\rho}{2}\int\int (v^2 + w^2)dS \quad (54)$$

The first integral term presents the viscous drag and the second integral term is the induced drag term.

$$\mathrm{D_i} = \frac{\rho}{2}\int\int (\mathrm{v}^2 + \mathrm{w}^2)\mathrm{dS} \quad (55)$$

Where v and w can be replaced [19] in terms of stream function and velocity potential function

$$v = \frac{\partial \Psi}{\partial z} + \frac{\partial \phi}{\partial y}, w = -\frac{\partial \Psi}{\partial y} + \frac{\partial \phi}{\partial z} \quad (56)$$

Substitute the v, w into induced drag term, the equation becomes

$$\mathrm{D_i} = \frac{\rho}{2}\int\int \left(\left(\frac{\partial \phi}{\partial y} + \frac{\partial \Psi}{\partial z}\right)^2 + \left(\frac{\partial \phi}{\partial z} - \frac{\partial \Psi}{\partial y}\right)^2\right) dS \quad (57)$$

After extending the equation, the entire equation can be divided into velocity potential group and stream function group.

$$D_{i,\phi} = \frac{\rho}{2}\int\int \left(\left(\frac{\partial \phi}{\partial y}\right)^2 + \left(\frac{\partial \phi}{\partial z}\right)^2\right) dS, and\ D_{i,\Psi} = \frac{\rho}{2}\int\int \left(\left(\frac{\partial \Psi}{\partial y}\right)^2 + \left(\frac{\partial \Psi}{\partial z}\right)^2\right) dS \quad (58)$$

The velocity potential group can be solved by changing the symbol.

$$D_{i,\phi} = \frac{\rho}{2}\int\int (\nabla\phi)\cdot(\nabla\phi)dS \quad (59)$$

As we know that $\nabla\phi \cdot \nabla\phi = \nabla \cdot \phi\nabla\phi$, the integration can be rewritten as

$$D_{i,\phi} = \frac{\rho}{2}\int\int \nabla \cdot \phi\nabla\phi dS \quad (60)$$

By using Green's Theorem, the simpler expression will be

$$D_{i,\phi} = \oint \phi \frac{\partial \phi}{\partial n} dl \tag{61}$$

Or a source term σ can be used to replace $\nabla \cdot \nabla \phi$

$$D_{i,\phi} = \frac{\rho}{2} \int \int \phi \sigma dS \tag{62}$$

Where $\sigma = \frac{\partial v}{\partial y} + \frac{\partial w}{\partial z} = \frac{\partial^2 \phi}{\partial y^2} + \frac{\partial^2 \phi}{\partial z^2} = \nabla \cdot \nabla \phi$.

The stream function group in equation (58) can also be solved with the same procedure, the equation is

$$D_{i,\Psi} = \frac{\rho}{2} \int \int \nabla \cdot \Psi \nabla \Psi dS \tag{63}$$

For the stream function, we use axial vorticity component ξ to simplify the equation.

$$D_{i,\Psi} = -\frac{\rho}{2} \int \int \Psi \xi dS \tag{64}$$

Where $\xi = \frac{\partial w}{\partial y} - \frac{\partial v}{\partial z} = -\frac{\partial^2 \Psi}{\partial y^2} - \frac{\partial^2 \Psi}{\partial z^2}$.

Hence, the induced drag can be expressed as

$$D_i = D_{i,\Psi} + D_{i,\phi} = -\frac{\rho}{2} \int \int \Psi \xi dS + \frac{\rho}{2} \int \int \phi \sigma dS \tag{65}$$

Note that we use positive axis to represent the induced drag, so the equation we use to calculate induced drag is

$$D_i = \frac{\rho}{2} \int \int \Psi \xi dS - \frac{\rho}{2} \int \int \phi \sigma dS \tag{66}$$

Takahashi [13] notes that the first term is the vorticial flow, and the second term is the strength of the residual closure flow in the wake.

To infer stream function Ψ and velocity potential function ϕ from test data, the common way is to solve the Poisson's equation [20] by the numerical methods such as the Jacobi method, Gauss-Seidel method, Successive Over-Relaxation (SOR), etc. The procedure is peculiar because solving the Poisson's equation means the test data needs to be differentiated twice. Normally, we prefer to integrate the data rather than differentiate them because of the effects of "noise". The differentiating data amplifies the effect significantly. Therefore, the Mclean's method on page 21 is more favorable to utilize in perspective of data post-processing.

$$\mathrm{D_i} = \iint_{S_1} \frac{1}{2}\rho\left(-\mathrm{u_{1_i}^2} + \mathrm{v_{1_i}^2} + \mathrm{w_{1_i}^2}\right)\mathrm{d}S_1 \tag{47}$$

C. Induced Drag Derivation: From Lifting Line Theory to VLM

Prandtl's Lifting Line Theory is a simplified model to predict the lift over a three-dimensional, finite wing with replacing it with a collection of "bound vorticity". As Anderson [8] states in "Fundamentals of Aerodynamics", the "induced drag" coefficient and lift coefficient can be derived with the concept of circulation and Kutta - Joukowski theorem which neglects thickness and camber effects.

$$\mathrm{C_{D_i}} = \frac{2}{V_\infty S}\int_{-\frac{b}{2}}^{\frac{b}{2}} \Gamma(y)\alpha_i(y)dy \tag{67}$$

$$\mathrm{C_L} = \frac{2}{V_\infty S}\int_{-\frac{b}{2}}^{\frac{b}{2}} \Gamma(y)dy \tag{68}$$

Where $\alpha_\mathrm{i}(y) = \alpha_i = \frac{\Gamma_0}{2bV_\infty}$ if the circulation varies elliptically along the span.

Hence, the induced drag can be presented in terms of lift coefficient.

$$C_{D_i} = \frac{C_L^2}{\pi AR} \tag{69}$$

So as induced angle of attack

$$\alpha_i = \frac{C_L}{\pi AR} \tag{70}$$

"Low-Speed Aerodynamics", [21] written by Joseph Katz & Allen Plotkin, mentions the same theory, but they extend the concept to a more general solution for a twisted wing.

Lifting Line Theory uses appropriate assumptions to predict the "induced drag" from downwash[8]. However, it only gives a realistic result for moderate to high aspect ratio because the assumption behind Lifting Line Theory is to replace a finite wing with a single lifting line across the span of the wing. Once the aspect ratio is larger, the assumption of single lifting line is closer to the actual situation. On the contrary, a finite wing has smaller aspect ratio, which is lower than four, can't be approached by only one lifting line since the chordwise variation is large enough that can't be seen as the same vortex.

For the wing such as swept wing, delta wing, or low aspect ratio wing like the test subject we use for comparison, Lifting Surface Theory developed by Multhopp [22][23] will be an alternative for a more precise result. Instead of replacing a finite wing with a lifting line, Lifting Surface Theory places many lifting lines at different chord points in Figure 10.

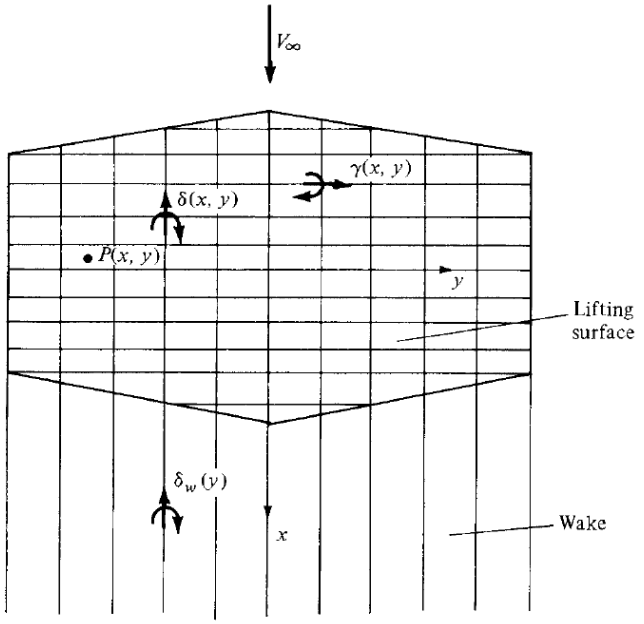

Figure 10: Concept of Lifting Surface Theory from "Fundamentals of Aerodynamics"[8]

This is different from the classical Prandtl's Lifting Line Theory because circulation and downwash are not only a function of spanwise location but also the chordwise location. The Vortex Lattice Method [10] is a numerical approach [22] to implement Lifting Surface Theory by computer, which is implemented in the VORLAX code [4]. It solves potential flows based on the vortex lattice method (VLM). However, these solutions apply only to purely inviscid flows, so the VORLAX's result is the tool used here to verify the characteristics of inviscid flow. It cannot capture viscous effects.

D. Proposed Induced Drag Corrections

All these elegant (and less elegant) derivations for finding "induced drag", with the exception of lifting surface theory, do not account for any geometry-dependent leading-edge suction in determining the induced drag, despite the phenomenon being well known as pointed out by Bertin & Cummings [24]. Nevertheless, there have been several authors who have attempted to correct the induced drag value based on this phenomenon, each through different methodologies. This thesis examines five different methods below.

1. Henderson's Leading-edge Suction Parameter

In 1966, William Henderson, who worked at NASA Langley, investigated the effect of leading-edge suction on wings with sharp leading-edges [25]. This was particularly relevant at the time due to said wings being considered during the development of a supersonic transport aircraft. The aim of this work was to simply determine how much leading-edge suction is being generated by the wing. To that end, Henderson defines a leading-edge suction parameter "*s*" as the percentage of observed suction to the amount of total possible suction. From Multhopp's [23] work on lifting surface theory, the drag is calculated as follows:

$$C_{D_i} = AR * \int_{-\frac{b}{2}}^{\frac{b}{2}} \Gamma \alpha_i dy \tag{71}$$

Note, once again, that this derivation neglects any axial force contribution to drag that might arise from thick or camber.

This calculation reduces to the value in Equation (7) given an elliptical loading:

$$C_{D_i} = \frac{C_L^2}{\pi * AR} \tag{72}$$

Equation (72) produces the lowest possible result for induced drag; that is, when the maximum suction occurs. The maximum drag-due-to-lift possible can be calculated in its most basic form simply as the entire streamwise component of lift:

$$C_{D_i} = C_L \tan \alpha \tag{73}$$

If the actual induced drag is less than this theoretical value, then there is some suction force that counterbalances the induced drag; thus, the difference between the total drag and the induced drag is the suction. Given that experimentally, drag-due-to-lift is simply the difference between total drag and zero-lift drag:

$$C_{D_{i,exp}} = C_D - C_{D_o} \tag{74}$$

The ratio of the suction forces can be simply defined as follows:

$$s = \frac{C_L \tan \alpha - \left(C_D - C_{D_o}\right)}{C_L \tan \alpha - AR * \int_{-\frac{b}{2}}^{\frac{b}{2}} \Gamma \alpha_i dy} * 100\% \tag{75}$$

While this is helpful for the determination of total suction generated out of the theoretical maximum for any given wing, the ratio does not offer any insight as to what properties of a wing generate this suction.

2. Polhamus: “Leading-edge Suction” Drag Coefficient Correlation

The same year Henderson’s paper was published, Edward Polhamus, a fellow colleague at NASA Langley, published a paper concerning the effect of leading-edge suction on the lift for a sharp leading-edge wing[26]. Two years later, in NASA TN D-4739 [26], Polhamus is following up his prior document to test his assumptions in the context of induced drag. Since his derivation of lift differs from previously discussed methods, we will first discuss the basics of his definition of lift before proceeding with his discussion of induced drag.

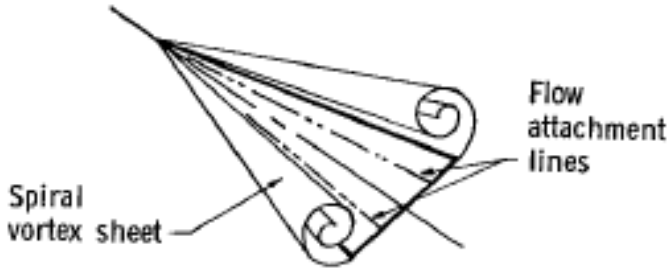

Figure 11: Polhamus Perspective[26]

Polhamus [26] examines lift from the perspective of a vortex generated in the fashion illustrated by Figure 11, whereby the leading-edge suction would propagate into the vortex sheet based on the leading-edge geometry. The lift coefficient is calculated as the sum of lift due to attached potential flow on the surface and lift due to the generated vortices; unlike some of the prior derivations, he attempts to do so without small angle approximation techniques. Based on the basic formulation of lift:

$$C_L = C_N \cos \alpha \tag{76}$$

Where the Equation (76) neglects the existence of axial force. The geometric relationship shows in Figure 12.

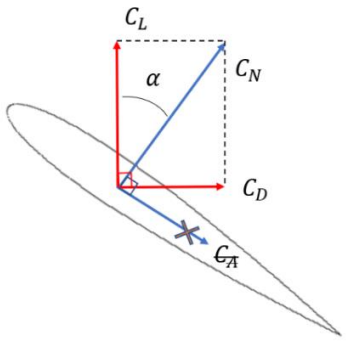

Figure 12: Neglect the Axial Force During the Derivation of Lift Coefficient.

Via the Kutta-Joukowski theorem, the normal force used for the potential flow is calculated to be as follows:

$$\mathrm{N} = \rho\Gamma\mathrm{b}(\mathrm{V}_\infty \cos\alpha) \tag{77}$$

The circulation here is defined as the total effective circulation, given by the following equation:

$$\Gamma = \mathrm{K_P}\frac{\mathrm{S_{ref}V_\infty}}{2\mathrm{b}}\sin\alpha \tag{78}$$

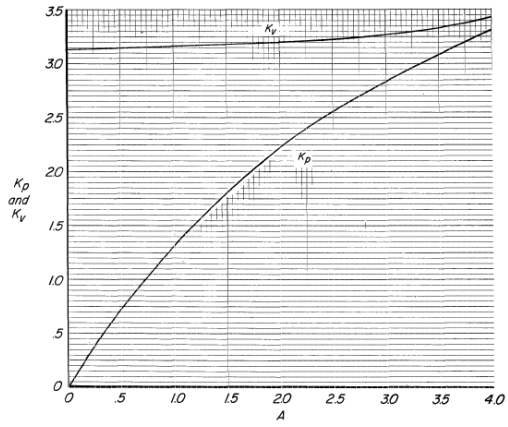

Figure 13: Kp versus Aspect Ratio[26]

In Polhamus's statement, the parameter K_p is determined as the lift-curve slope with the assumption of small angle approximations, which the author obtains from a modified Multhopp lifting-surface theory [22]; the relationship is shown visually in Figure 13 as a function of wing aspect ratio.

However, compare with the general form of circulation's equation mentioned in previous section:

$$\Gamma(\theta) = \Gamma_0 \sin\theta = \frac{2V_\infty S_{ref} C_L}{b\pi} sin(\theta) \tag{25}$$

$$\Gamma = \int_0^\pi \Gamma(\theta) d\theta = \frac{4V_\infty S_{ref} C_L}{b\pi} \tag{79}$$

$$C_L = \frac{\pi}{8} K_p \sin\alpha \approx \frac{\pi}{8} K_p \alpha, \qquad \text{if } \alpha \text{ is a small angle.} \tag{80}$$

The equation above shows the statement of $C_L = K_p\alpha$ from Polhamus [26] is not precise. The parameter K_p is not the slope of lift-curve. Instead, $\frac{\pi}{8}K_p$ should be the lift-curve slope. Hence, even the comparison shows the $C_L = K_p\alpha$ statement is not correct, we still can use the concept of K_p to correct the leading-edge effect.

By substituting the circulation into the normal force equation and reducing it to coefficient form, the following equations for normal force coefficient and lift coefficient can be derived:

$$C_{N_P} = K_P \sin\alpha \cos\alpha$$

$$C_{L_P} = K_P \sin\alpha \cos^2\alpha \tag{81-82}$$

The discussion of drag Polhamus reiterates that the $\sin\alpha$ term accounts for the true boundary condition and the $\cos^2\alpha$ term enforces the Kutta condition. The normal force coefficient for the vortex lift case is taken to be the suction coefficient C_S which is perpendicular to the leading edge, related to the thrust coefficient C_T, which is paralleled to the incoming wind, by the leading-edge sweep angle of the wing:

$$C_{N_V} = C_S = \frac{C_T}{\cos\Lambda} \tag{83}$$

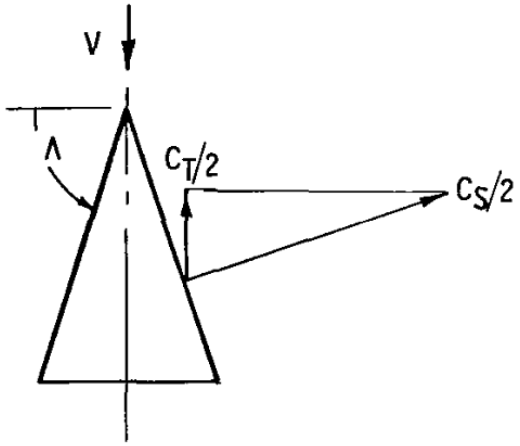

Figure 14: Relationship Between Cs and C_T from Polhamus's paper [26]

The thrust and thrust coefficient (with Equation (73) substituted appropriately) are shown below:

$$T = \rho\Gamma(V_\infty \sin\alpha - w_i)$$

$$C_T = \left(1 - \frac{w_i}{V_\infty \sin\alpha}\right) K_P \sin^2\alpha \tag{84-85}$$

Where w_i refers to the downwash velocity normal to the chord. Based on the proportionality of w_i and Γ, as well as Γ to $V_\infty \sin\alpha$, Polhamus deduces that the ratio

$\frac{w_i}{V_\infty \sin\alpha}$ is independent of α and can be equated to parameters derived from lift theories that rely on small-angle approximations (despite his attempt to refrain from said approximations). Given the parameter K_i, defined as follows:

$$K_i = \frac{\partial C_{D_i}}{\partial C_L^2} \tag{86}$$

The ratio $\frac{w_i}{V_\infty \sin\alpha}$ is then defined:

$$\frac{w_i}{V_\infty \sin\alpha} = K_P K_i \tag{87}$$

Polhamus claims that any currently accepted form of the induced drag slope (such as $\frac{1}{\pi AR * e}$ from the derivation in Section B, Part 2) can be utilized. He personally uses Multhopp's variation. Substituting Equation 81 into Equation 78, and subsequently Equation 78 into Equation 76 and Equation 76 into Equation 71, results in the following equations:

$$C_T = (K_P - K_P^2 K_i)\sin^2\alpha$$

$$C_{L_V} = (K_P - K_P^2 K_i)\frac{\cos\alpha}{\cos\Lambda}\sin^2\alpha \tag{88-89}$$

The parameter $K_V = (K_P - K_P^2 K_i)\frac{1}{\cos\Lambda}$ is then defined for the sake of convenience; the variation of this parameter is shown in Figure 15.

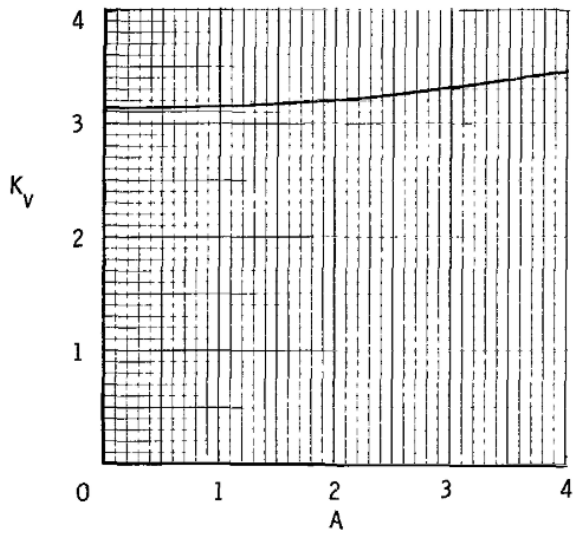

Figure 15: Variation of K_v with Aspect Ratio for Sharp-edge Delta Wings from Polhamus's Paper[26].

The final vortex lift, and total lift are as follows:

$$C_{L_V} = K_V \sin^2 \alpha \cos \alpha$$

$$C_L = C_{L_P} + C_{L_V} = K_P \sin \alpha \cos^2 \alpha + K_V \cos \alpha \sin^2 \alpha \qquad (90-91)$$

Polhamus [26] notes that the term $K_V \sin \alpha$ in Equation (85) represents the leading-edge suction, with the $\cos \alpha$ term orienting the suction in the direction of lift.

When examining drag, the drag-due-to-lift is then defined as the axial component of lift as shown below:

$$C_{D_i} = C_L \tan \alpha \qquad (92)$$

Which the equation neglects axial force term.

Polhamus [26] then considers three cases: the first case is where there would be zero leading-edge suction with vortex lift (despite the fact that vortex lift was originally defined in terms of leading-edge suction):

$$C_{D_i} = C_L \tan\alpha = K_P \sin^2\alpha \cos\alpha + K_V \sin^3\alpha \tag{93}$$

The second case considers zero leading-edge suction with only potential flow lift:

$$C_{D_i} = C_{L_P} \tan\alpha = K_P \sin^2\alpha \cos\alpha \tag{94}$$

Lastly, the third case assumes full leading-edge suction, where the induced drag is assumed to be equal to Equation (7) reiterated below:

$$C_{D_i} = \frac{C_L^2}{\pi * AR} \tag{7}$$

What is of particular interest is Polhamus's findings that the drag-due-to-lift for a sharp leading-edge delta wing most closely follows case 1 shown above in Equation 91. This implies, as Polhamus duly notes, that the sharp leading-edge wing does not produce leading-edge suction.

However, the paradox is that the vortex lift is derived based on the assumption that leading edge suction does indeed exist! This is discussed and postulated to be a result of a rotation of the suction vector such that the vortex lift is generated but thrust, which would reduce drag, is not. This is reiterated by Carlson, Mack & Barger [27] in their estimation of the thrust itself, discussed below in the next section.

3. Pressure Loops and the Concept of Leading-edge Suction

Leading Edge suction is an axial (or drag direction) force contribution due to the interaction of the nuanced thickness, incidence and camber profile of the wing, and the local surface pressures resulting from flow over this surface. This effect was originally noted by the Bairstow and Jones in ARC R&M 60 from 1914[16].

Instead of the classical Cp vs chordwise location pressure plot (see Figure 16), we consider the projection of the pressures in terms of the wind-axis frontal area of the lifting surface (see Figure 17)

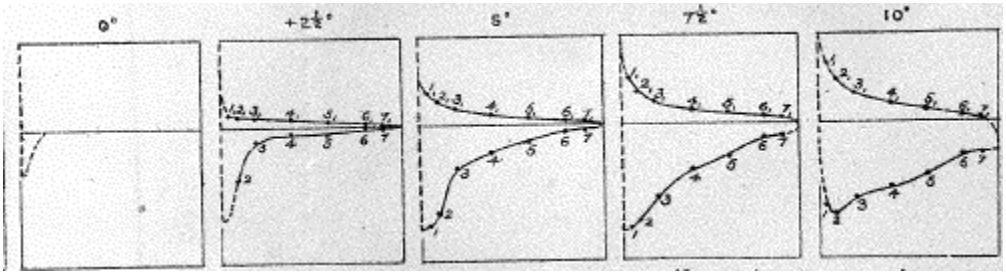

Figure 16: Classical CP vs Chord Plot (from ARC R&M 60)

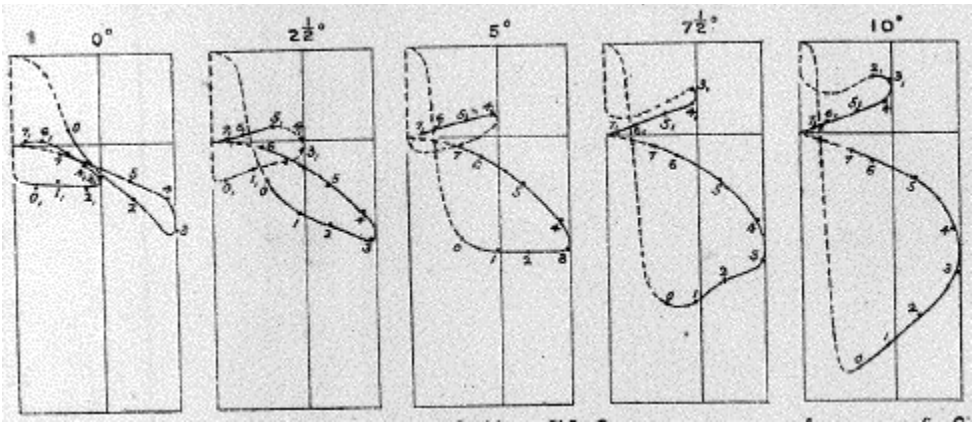

Figure 17: Suction Loop CP vs Z' Plot (from ARC R&M 60)

The manifestation of these forces from the nuanced thickness can be seen in Figure 18, Figure 19, Figure 20, and Figure 21

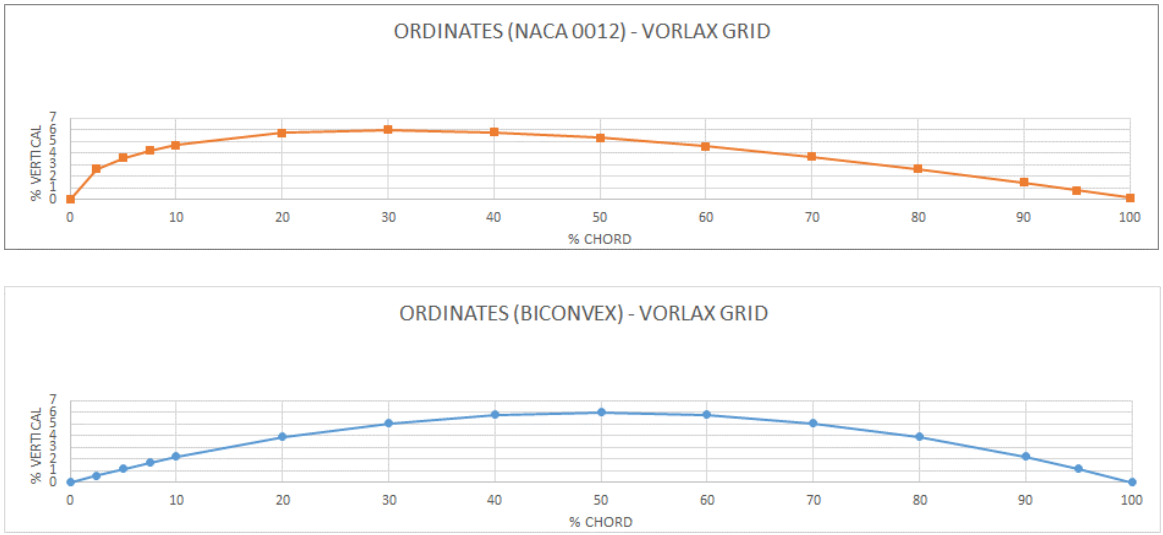

Figure 18: NACA 0012 and Biconvex Airfoil Coordinates

In Figure 18, we plot the geometry of a typical NACA 0012 airfoil and the biconvex airfoil. In Figure 19, we compute the direction cosines from the geometry, this represents the fraction of the pressure acting in the direction normal to the airfoil reference chord. While the integration of this value produces a value close to 1, it is not exactly 1. We also compute the direction sines from the geometry; this represents the fraction of the pressure acting in the direction aligned with the airfoil reference chord – in other words in the axial direction. Thus, airfoils produce a “pressure drag” or “pressure thrust” even in the absence of sonic or separated flow.

In Figure 20, we compute the direction cosines and sines from the geometry in the wind axis at an angle-of-attack of 5-deg. This highlights how the upper and lower pressures developed by the wing develop pressure "drag" forces – all completely ignored by lifting line theory.

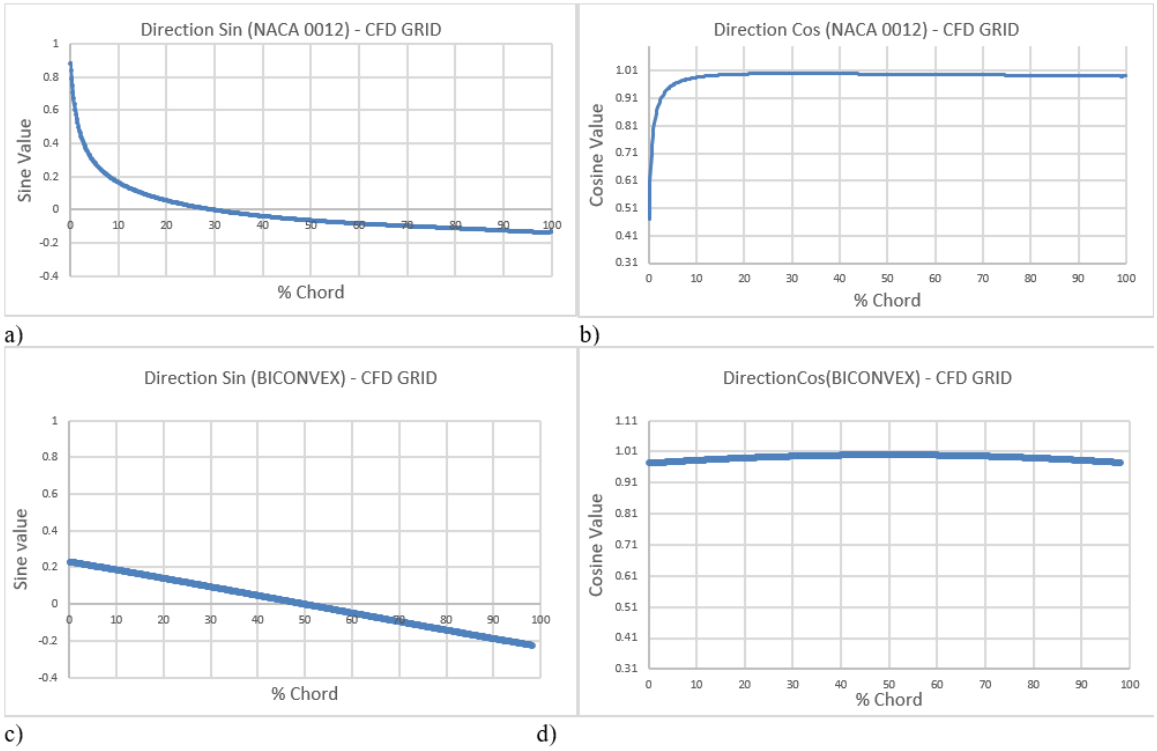

Figure 19: Comparison of Cosine and Sine Components for the Normal Vector of the Mesh Panels Between a NACA 0012 Airfoil and a Biconvex Airfoil.

These four plots show the cosine and sine components on each mesh panel generate by CFD software. Figure a and b are for a NACA 0012 airfoil. Figure c and d are for a biconvex airfoil.

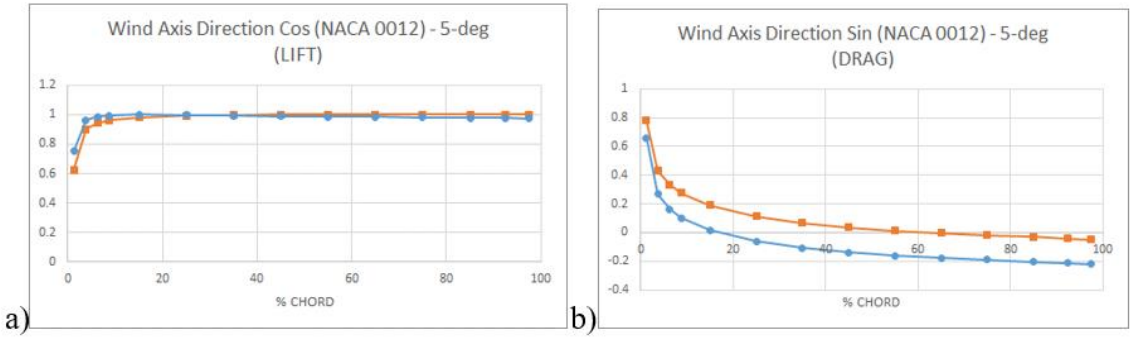

a) b)

Figure 20: Direction Cosines NACA 0012 Airfoil at 5-degree Angle of Attack.

4. Analytical Correction as applied to Vortex Lattice Calculations

Since the planform of the airfoil is getting more complicated, the vortex lattice method is used for computer program to deal with the complex calculation. VORLAX code generates a fully attached, steady, inviscid, small perturbation flow with either purely subsonic or supersonic condition. To include the compressibility effect, the Prandtl-Glauert correction factor is applied to the vortex lattice calculation.

$$\beta = \sqrt{1 - M_{\infty}^2} \tag{95}$$

How to apply it in physical meaning? There are many explanations for elaborating the geometry deformation of Prandtl-Glauert effect collected in Kirkman & Takahashi's paper [28]. In VORLAX, it takes the concept of Jones & Cohen's explanation for computation. The transformation stretches the chord of an airfoil, which is in the x-coordinates, by a factor of $\frac{1}{\sqrt{1-M^2}}$ to simulate the wing surrounded by an incompressible flow.[29] They mention that span is identical during Prandtl's transformation, but the effective area becomes larger because of the stretching of the chord. Therefore, if the Mach

number gradually approach to one, the chord of the corresponding wing incompressible flow turns out to be infinitely long in comparison with the span and the characteristic of flow grow essentially into two-dimensional [27].

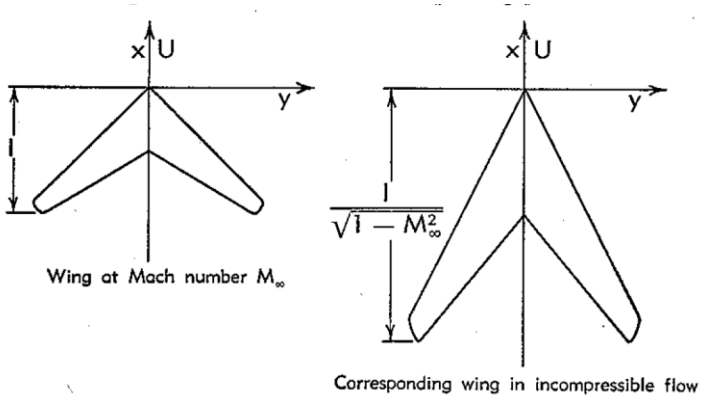

Figure 21: Geometry Stretching of Prandtl-Glauert Transformation(from Jones's Book[30])

To discuss the effect of leading-edge suction, a three-dimensional effect, in the flow field, this study places emphasis only on the subsonic flow to maximize the effect presented.

Thickness is another issue for the vortex lattice system. A code utilizing panels method can't generate a model with thickness because all the vortex lattices are considered as infinitely thin. Although the model can't have any thickness, the thickness effects can be simulated by a double vortex lattice layer which we call it "sandwich" panel model described in the VORLAX manual [4]. The two layers will interfere with each other and act as a thick airfoil.

Since the code uses the vortex lattice method, sideslip effects are excluded from it, which there must have some correction applied here. The effect usually can be computed by two different approached depended on the coordinated system. Skewed-wing approach and skewed free-stream approach [4]. The first one establishes in the wing axis, so the longitudinal axis is the freestream vector and skewed free-stream approach is based on the body axis, which shows in Figure 22. Instead of using either of the approaches, VORLAX combines both methods to reduce the cost of computation.

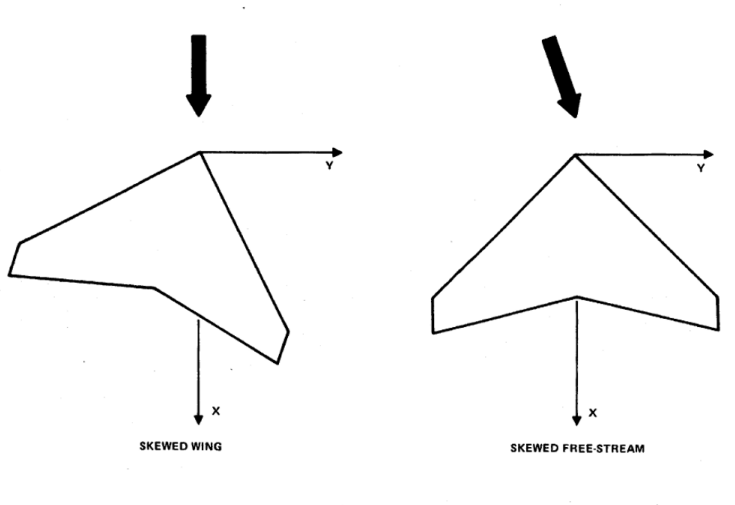

Figure 22: Two Approaches to Calculate Sideslip Effect

The key point of this thesis paper is to verify the relationship of induced drag and different leading edge. However, the leading edge suction in VORLAX is controlled by a variable called SPC which it can be either fully turned on or off. The blunt leading-edge can be simulated by SPC being set equal to 1, but the sharp leading-edge should have few leading-edge suction instead of no leading-edge suction. To correct the problem, the linear interpolation can roughly approach the result we need. Applying a certain ratio of leading-

edge suction by comparing with CFD result can produce the inviscid result for biconvex airfoil from VORLAX. Based on our CFD data for the biconvex airfoil, the leading-edge suction for it is 30 percent of full leading-edge suction in Figure 23.

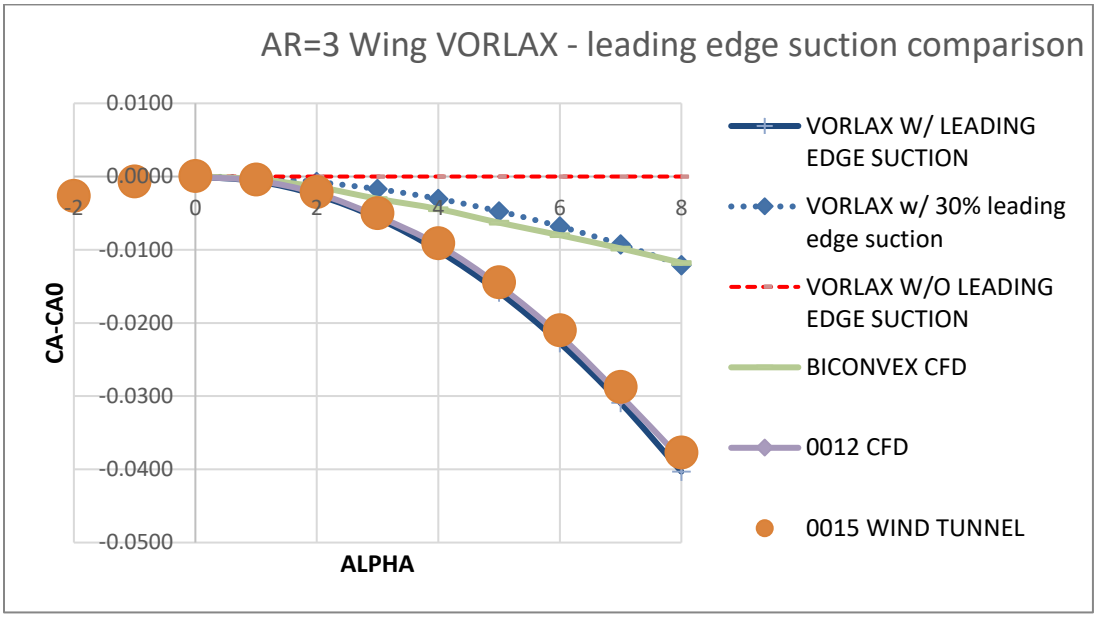

Figure 23: Leading-Edge Suction Correction

MODELS AND RAW DATA

A. Description of Wind Tunnel Test

According to the Morrow's experimental data[31][32] is post-processed by Takahashi, the lift coefficient and drag coefficient versus alpha can be found in Figure 24 and Figure 25.

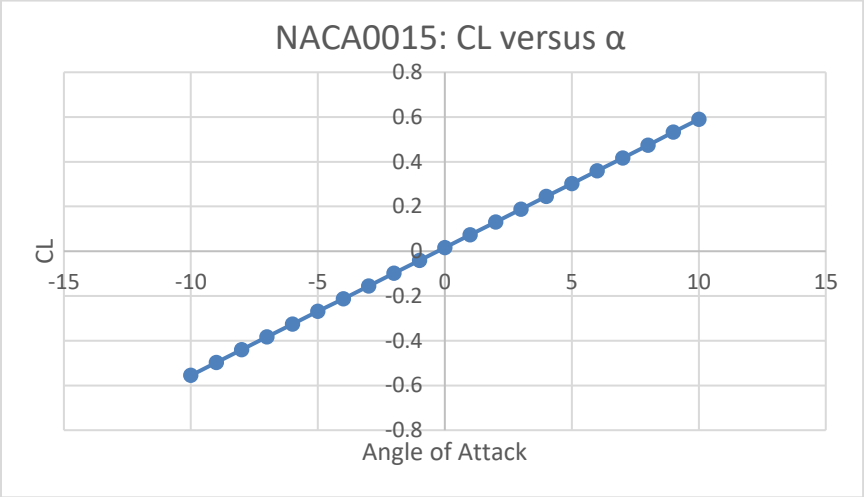

Figure 24: NACA0015: CL versus α

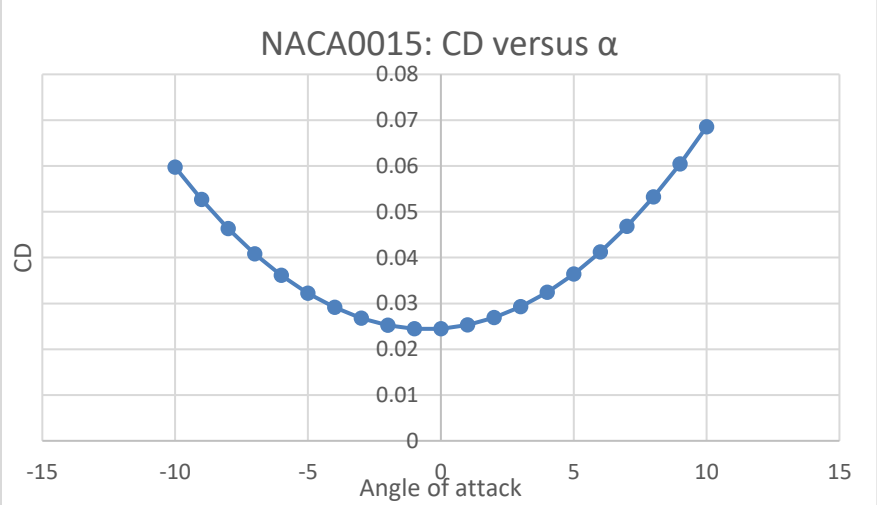

Figure 25: NACA0015: CD versus α

Since the experimental data is a tool to verify the CFD result in this study, we combine the two figures into drag polar plot in Figure 26. The discussion and comparison of multiple data sets will be discussed in the "RESULTS AND DISCUSSION" section.

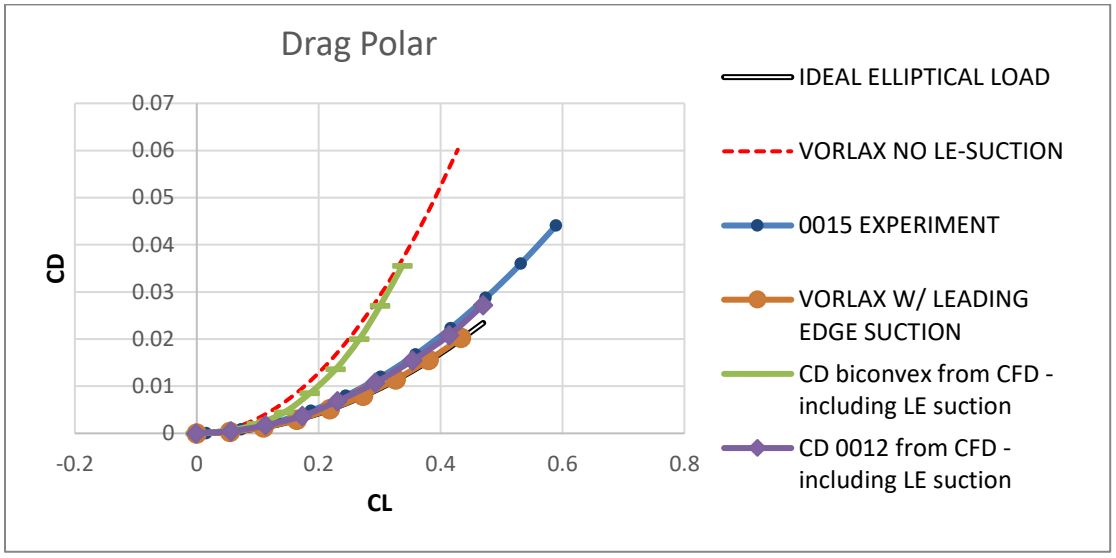

Figure 26: Drag Polar with Experimental Data

B. Description of Flat Plate VORLAX Model

Vortex lattice method (VLM) is based on the lifting surface theory which uses vortex to replace a finite wing. The thin flat plate model is one of the useful tools to predict the aerodynamic features of an airfoil. In the left of Figure 27, the plot shows how VORLAX code processes a finite wing into a thin panel lattice.

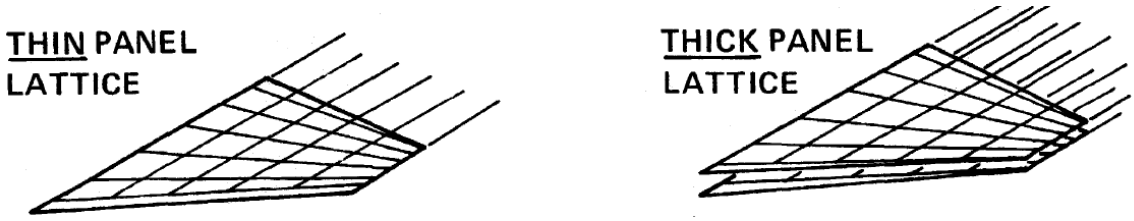

Figure 27: Panels Lattice for Thin Plate Model and Sandwich Model[4]

According to the manual of VORLAX [4], we can setup our input file in Figure 28. It is notable that we utilize the symmetric boundary condition so there is only half wing in the setup. Besides, the crucial variable for this study is the leading-edge suction term since the planform will be the same if we don't consider the thick-wise of the wings. To make the difference, leading-edge suction is an important factor to control. We do full leading-edge suction for simulating a blunt leading-edge wing and the no-leading-edge suction for predicting a sharp leading-edge wing. The key variable is SPC which is described as a leading-edge suction multiplier in VORLAX [4]. Comparing Figure 28 and Figure 29, the two setups are almost the same but SPC term is different. The leading-edge suction multiplier can be turned on by setting the SPC equal to 1.

```
*ISOLV     LAX       LAY      REXPAR    HAG       FLOATX    FLOATY        ITRMAX
 0         0         0        0.2       0         0         0                399
*NMACH    MACH
 1        0.1
*NALPHA   ALPHA
 9       0 1 2 3 4 5 6 7 8
*LATRL    PSI       PITCHQ    ROLLQ     YAWQ      VINF
 0        0         0         0         0         1
*NPAN     SREF      CBAR      XBAR      ZBAR      WSPAN
 1        48.0      4.0        1.0      0.0       12.0
*-------------------------------------------------------------------------------
*Panel #1 Wing
*X        Y         Z         CORD
0.0       0.0       0.0       4.0
0.0       6.0       0.0       4.0
*NVOR     RNCV      SPC       PDL
50        20        1.0         0
*AINC1    ANINC2    ITS       NAP        IQUANT    ISYNT     NPP
0         0         0         0          0         0         0
* NXS     NYS       NZS
  00      00        00
```

Figure 28: Full Leading-edge Setup for an Aspect Ratio 3 Airfoil.

```
*ISOLV     LAX       LAY      REXPAR    HAG       FLOATX    FLOATY        ITRMAX
 0          0         0        0.2       0         0         0               399
*NMACH    MACH
 1        0.1
*NALPHA   ALPHA
 9       0 1 2 3 4 5 6 7 8
*LATRL    PSI       PITCHQ    ROLLQ     YAWQ      VINF
 0        0         0         0         0         1
*NPAN     SREF      CBAR      XBAR      ZBAR      WSPAN
 1        48.0      4.0        1.0      0.0       12.0
*-------------------------------------------------------------------------------
*Panel #1 Wing
*X        Y         Z         CORD
0.0       0.0       0.0       4.0
0.0       6.0       0.0       4.0
*NVOR     RNCV      SPC       PDL
50        20        0         0
*AINC1    ANINC2    ITS       NAP        IQUANT    ISYNT     NPP
0         0         0         0          0         0         0
* NXS     NYS       NZS
  00      00        00
```

Figure 29: No Leading-edge Setup for an Aspect Ratio 3 Airfoil.

However, the wing we want to compare is biconvex which has some leading-edge suction instead of full or zero. Without the resort the apply “some” leading-edge suction to flat plate model, we interpolate the full leading-edge suction case and no leading-edge suction case to fit the data acquired from Autodesk CFD. In Figure 30, the VORLAX result with 30% leading-edge suction seems to fit the CFD result well.

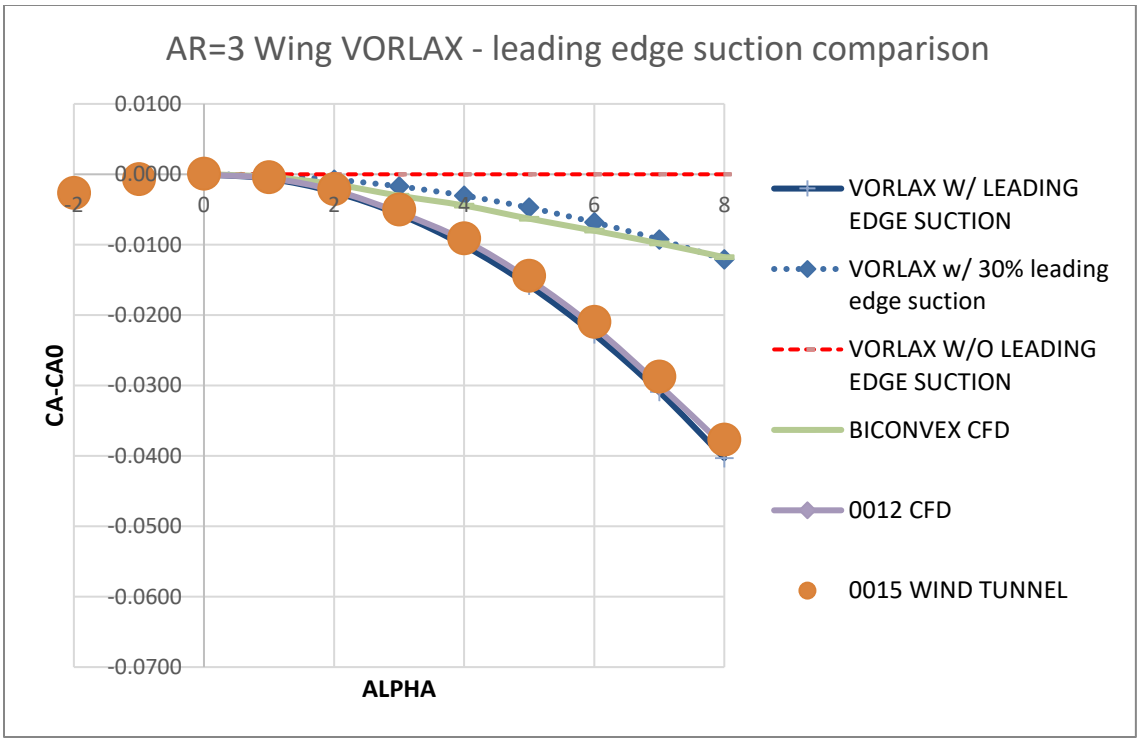

Figure 30: Leading-edge Suction Comparison

Full leading-edge suction		No leading-edge suction		30% Leading edge suction	
CL	CDi	CL	CDi	CL	CDi
0	0	0	0	0	0
0.05474	0.00032	0.05473	0.00096	0.05473	0.00077
0.10943	0.00129	0.10934	0.00382	0.10936	0.00306
0.16401	0.00289	0.16371	0.00858	0.1638	0.00687
0.21845	0.00512	0.21774	0.01523	0.21796	0.0122
0.27269	0.00799	0.27131	0.02374	0.27173	0.01901
0.32668	0.01147	0.32431	0.03409	0.32502	0.0273
0.38039	0.01557	0.37662	0.04624	0.37775	0.03704
0.43376	0.02026	0.42815	0.06017	0.42983	0.0482

Table 1: VORLAX Flat Panel Result

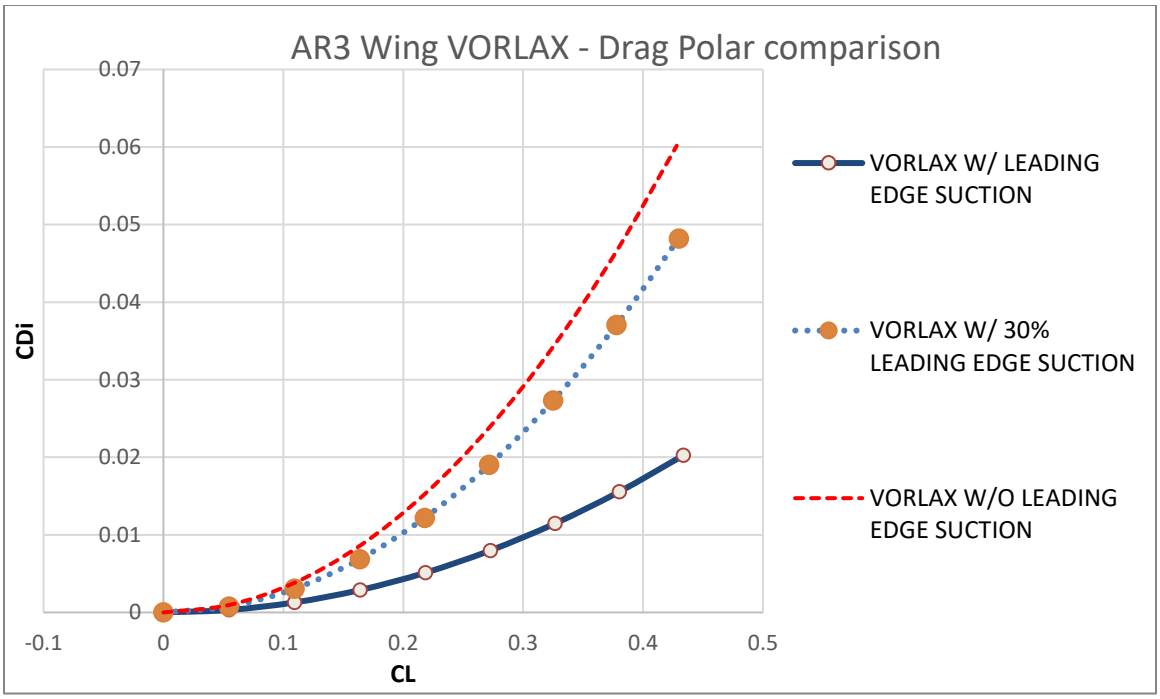

Figure 31: VORLAX Drag Polar Comparison

The comparison of full, no, 30% leading-edge suction shows in Table 1 and Figure 31: VORLAX Drag Polar Comparison.

C. Description of Thick "Sandwich" VORLAX Model

The "sandwich" panel is the two semi-impermeable lattice layers used to model the thick wing (see the right-hand-side sketch in Figure 27). While a double impermeable single lattice later model can provide a reliable data set, it can only compute the pressure difference between the upper surface and the lower surface. To plot the pressure loop and pressure distribution, the pressure data is necessary for then. The sandwich model uses two lattice layers to simulate the upper and lower surfaces of the wing. The distance between two lattice panels can't be too close or too far. Too close will cause the convergence

problem, and too far will make the two panels become independent. Therefore, finding a proper distance is a try-and-error process. To setup sandwich panel model, we need more than the planform of a wing. Camber of each panel is a factor to control the curvature of the surface. The camber of upper and lower surface of a NACA0012 and a Biconvex wing show in Table 2 and Table 3.

X/C	UPPER SURFACE	LOWER SURFACE
0.0	0.0000	-0.0000
2.5	2.6150	-2.6150
5.0	3.5550	-3.5550
7.5	4.2000	-4.2000
10.0	4.6830	-4.6830
20.0	5.7370	-5.7370
30.0	6.0020	-6.0020
40.0	5.8030	-5.8030
50.0	5.2940	-5.2940
60.0	4.5630	-4.5630
70.0	3.6640	-3.6640
80.0	2.6230	-2.6230
90.0	1.4480	-1.4480
95.0	0.8070	-0.8070
100.0	0.1260	-0.1260

Table 2: Surface Ordinates Distribution for a NACA0012 Wing

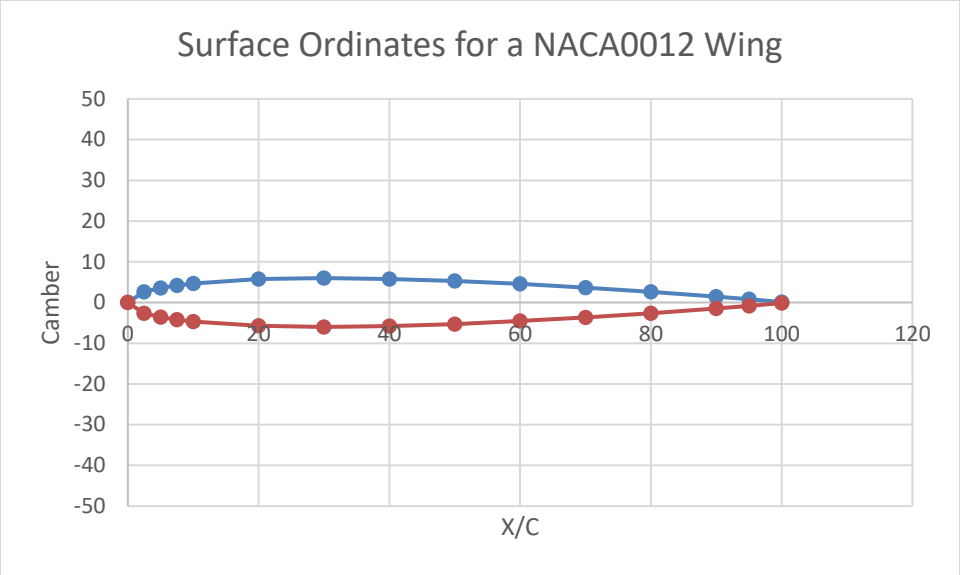

Figure 32: Surface Ordinates Distribution for a NACA0012 Wing

X/C	UPPER SURFACE	LOWER SURFACE
0.0	0.0000	0.0000
2.5	0.5927	-0.5927
5.0	1.1534	-1.1534
7.5	1.6824	-1.6824
10.0	2.1800	-2.1800
20.0	3.8598	-3.8598
30.0	5.0515	-5.0515
40.0	5.7633	-5.7633
50.0	6.0000	-6.0000
60.0	5.7633	-5.7633
70.0	5.0515	-5.0515
80.0	3.8598	-3.8598
90.0	2.1800	-2.1800
95.0	1.1534	-1.1534
100.0	0.0000	0.0000

Table 3: Surface Ordinates Distribution for a Biconvex Wing

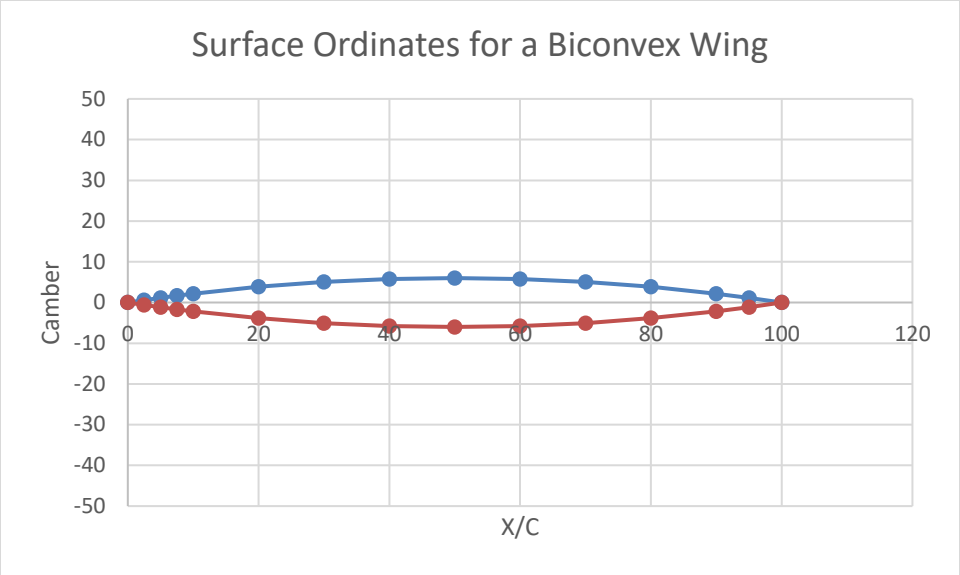

Figure 33: Surface Ordinates for a Biconvex Wing.

One thing that needs to be made aware of is that the drag coefficient from VORLAX output file for a "sandwich" model can't be trusted if we turn on the leading-edge suction multiplier. The possible reason for this output is that the code adds a double leading-edge suction to the entire wing because there are two lattices layer, thus, the drag coefficients are all negative, which means there is no drag, no matter what angle of attack. However, we can still get the result from Mclean's Wake survey and compare with the data from Autodesk CFD.

D. Description of AUTODESK CFD Model

Autodesk CFD 2018 is an industrial software used in fluid dynamics. It provides several solvers utility in different circumstances. To test the precision of the software and each turbulent model for our blunt leading-edge and sharp leading-edge case, a benchmark is needed.

In Autodesk CFD 2018, there are 10 different turbulent models: k-epsilon, SST k-omega, SST k-omega SAS, SST k-omega RC(Smirnov-Menter), SST k-omega (Hellsten), SST k-omega DES, RNG, Low RE k-epsilon, Mixing Length, Eddy Viscosity. Based on the description in Autodesk CFD official website [33], the possible models for simulating the fluid we need are SST series. Also, according to the situation we need to test the two leading-edge cases, a steady-state, three-dimensional, turbulent external flow across a cylinder is the simplest model to run the simulation. The result-oriented method is then utilized to verify which turbulent model we should use for our test subject. The result listing in Table 4 shows SST k-omega RC (Smirnov-Menter) got the result which is closest to the benchmark value with $\pm$0.76% error.

Turbulent models	**Coarse mesh**		**Finer mesh**	
	Force	C_D	Force	C_D
K-epsilon	43.822	1.599(±75%)		
SST	29.341	1.071(±18%)	27.435	1.001(±10%)
SST RC SM	29.186	1.065(±17%)	24.7372	0.903(±0.76%)
SST RC H	28.969	1.057(±21%)	24.167	0.882(±3.08%)
SST DES	31.725	1.158(±27%)		
SST SAS	31.528	1.150(±26%)		
Benchmark is $C_D = 0.91$				

Table 4: Turbulent Models Test

To understand the influence of leading-edge geometry, other controlled variables need to be fixed. The two test subjects should have an identical chord, span, thickness, and they are tested under the same flow setup.

Geometry Setup

Chord: 4 inches

Span: 12 inches

Thickness: 12% (NACA0012 for blunt leading-edge airfoil)

Control Volume: 10 inches * 20 inches (Using symmetry boundary condition to simplify the model.)

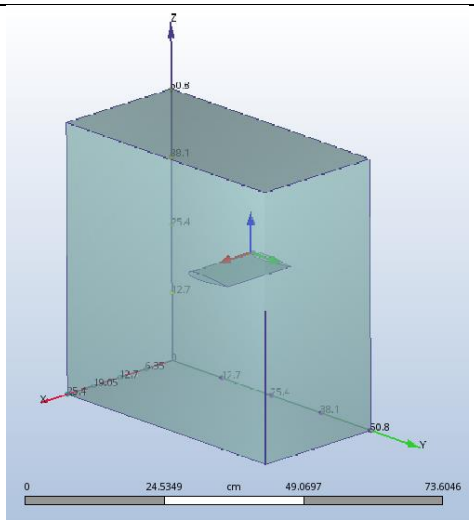

Figure 34: Geometry Setup

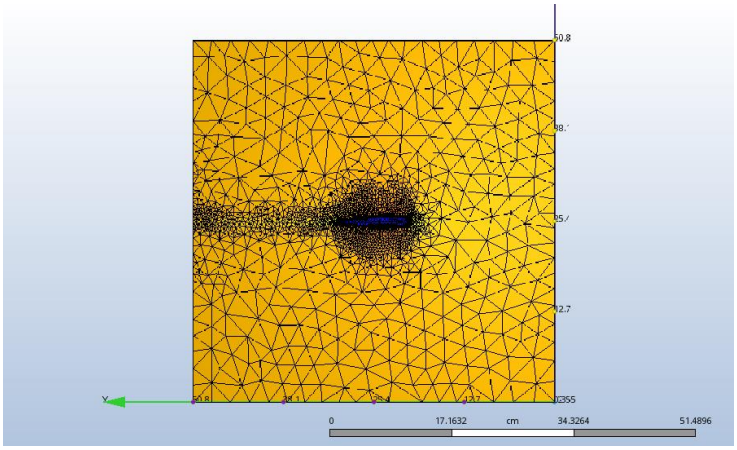

Figure 35: Mesh Around the Airfoil

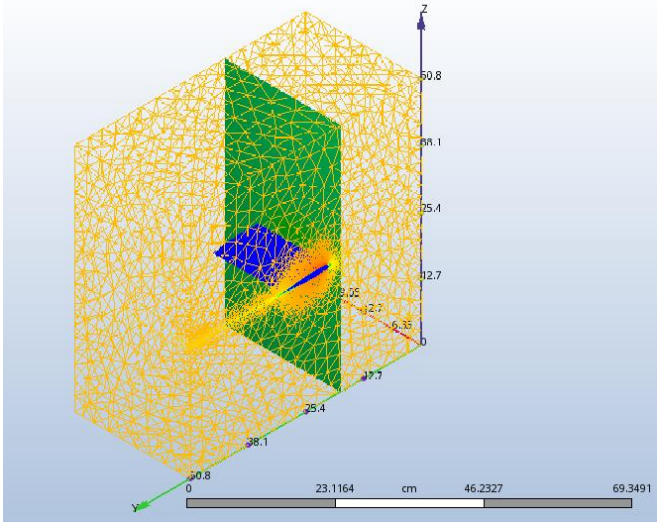

Figure 36: Wireframe for Control Volume

Simulation Setup

Range of Angle-of-Attack: 0~8 degrees

Boundary Condition: 30 m/s in the inlet, 0 Gage pressure in the outlet, and Slip/Symmetry condition in the other four walls to simulate an unlimited wide wind tunnel.

Solution Mode: Steady state.

Turbulent Model: SST k-omega RC (Smirnov-Menter)

Wall Layers: 15 layers with 0.45-layer factor and wall layer blending enabled.

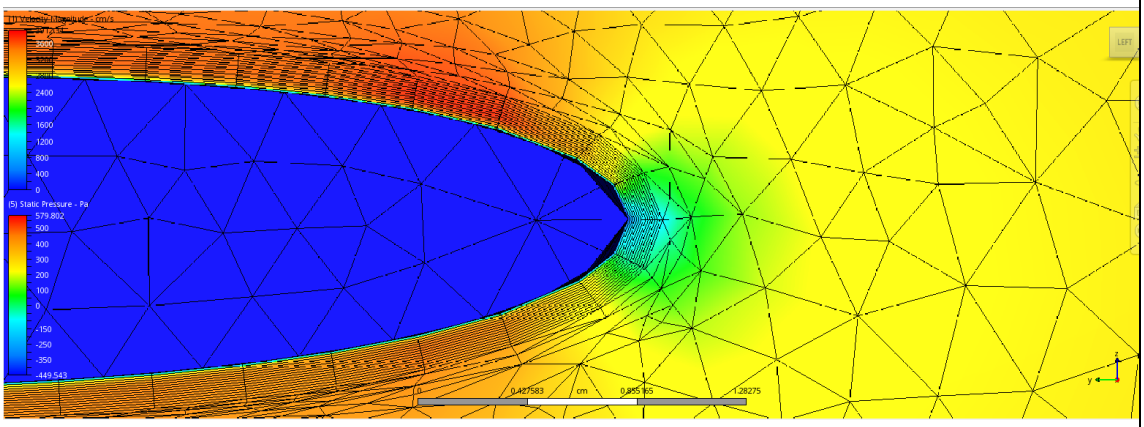

Figure 37: Wall Layers

To make sure our computational results converge to a valid answer, it is best to make a convergence plot. From Figure 38, the residual value should be close to zero when the model has fully converged. In this figure, Vx, Vy, Vz are the velocity components, *Press* is the pressure, *Temp* is the temperature, *TKE* represents the turbulent kinetic energy, *TED* shows the turbulent energy dissipation, and *Scalar* is the value for showing if turbulent viscosity exists; which is indicated when *Scalar* = 1. In the residual convergence

plot, we look at the velocity components and pressure value. They are faded to zero as the number of iterations goes up, which means the result is converged properly.

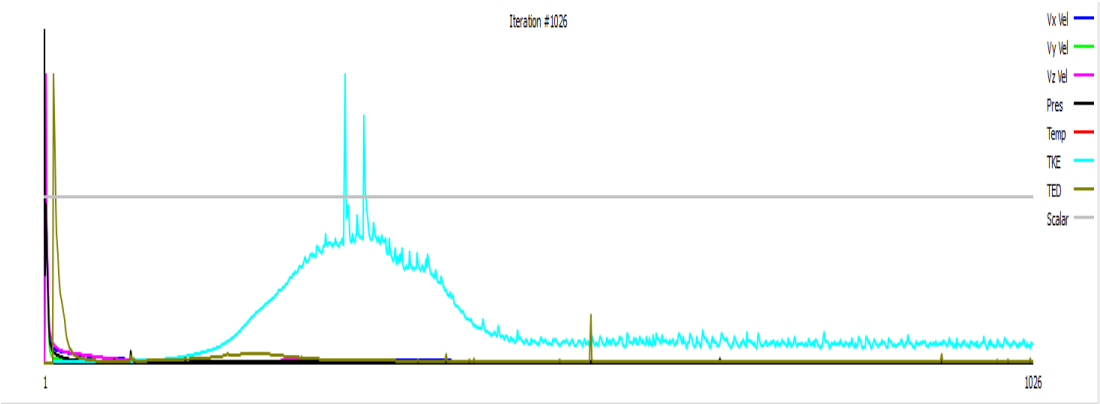

Figure 38: Convergence Plot (Residual)

Other than residual value, the potential velocity change is also an interesting value to look at. For a steady state condition, the energy tends to become smaller as the model converges. The phenomena can present in the potential velocity because of the kinetic energy. From Figure 39, the all velocity components become the small values in the end of computation. That is another evidence that the CFD result has fully converged.

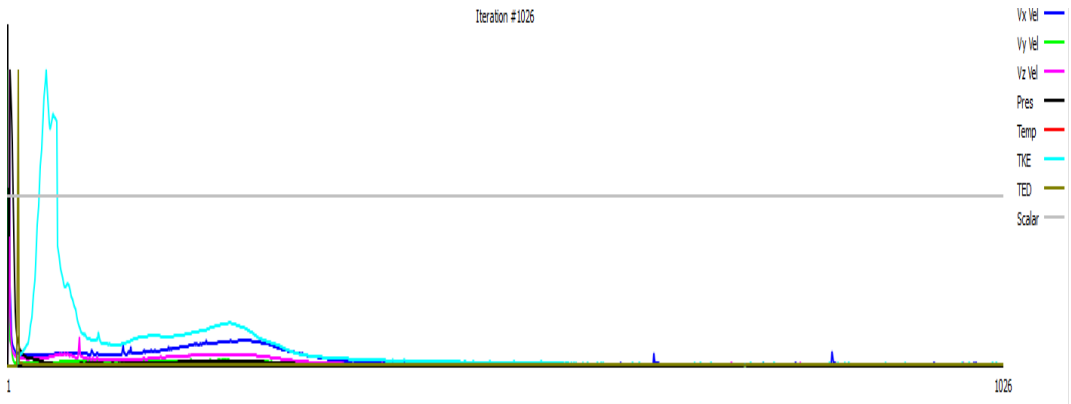

Figure 39: Convergence Plot (DPhi/Phi)

Aside from these two kinds of convergence plots, we can show an intuitive graph with Figure 40. It shows how all values stabilize after many iterations; this indicates convergency because our model is supposed to be steady state.

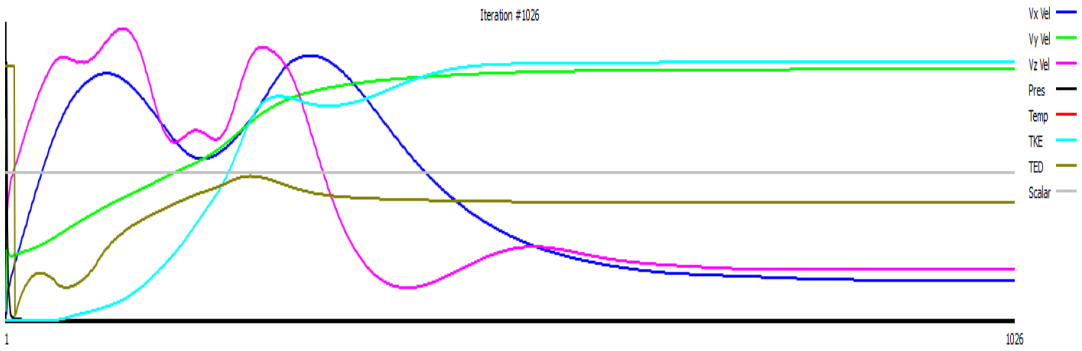

Figure 40: Convergence Plot (Average)

The figures of two cases with nine different angles are Figure 41 and Figure 42, which shows the velocity field under several circumstances. As angle-of-attack increases, the blunt leading-edge can accelerate the flow across the upper surface of the airfoil earlier. Relatively, the sharp leading-edge has lower speed when it reaches the high angle-of-attack. It causes flow separation to happen in the trailing edge easily. However, the pitch angle is not high enough to see the severe separation from the velocity field or pressure field in Figure 43 and Figure 44.

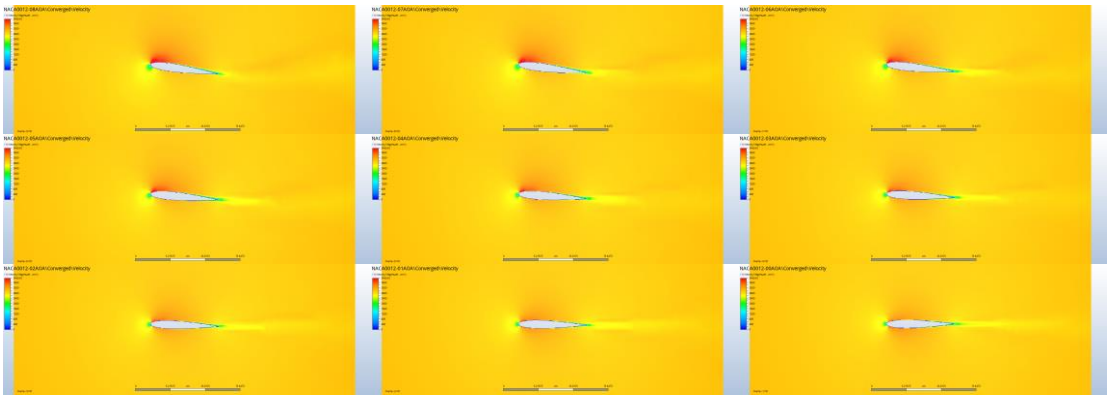

Figure 41: Velocity Field for a NACA0012 Airfoil from Zero to Eight Angle of Attack

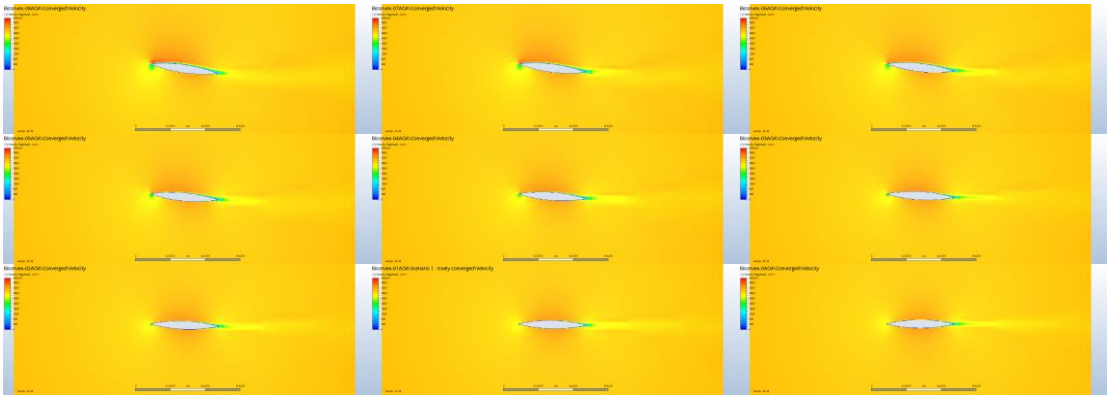

Figure 42: Velocity Field for a Biconvex Airfoil from Zero to Eight Angle of Attack.

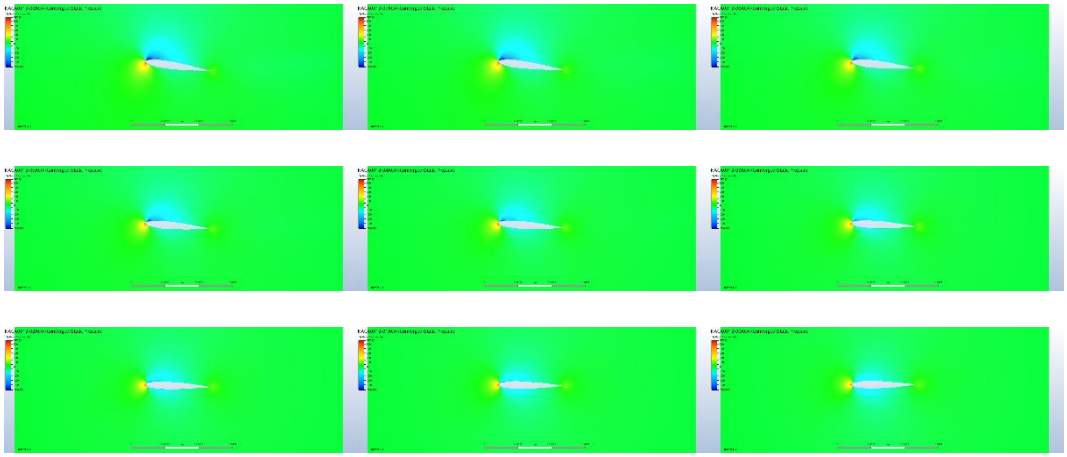

Figure 43: Pressure Field for a NACA0012 Airfoil from Zero to Eight Angle of Attack

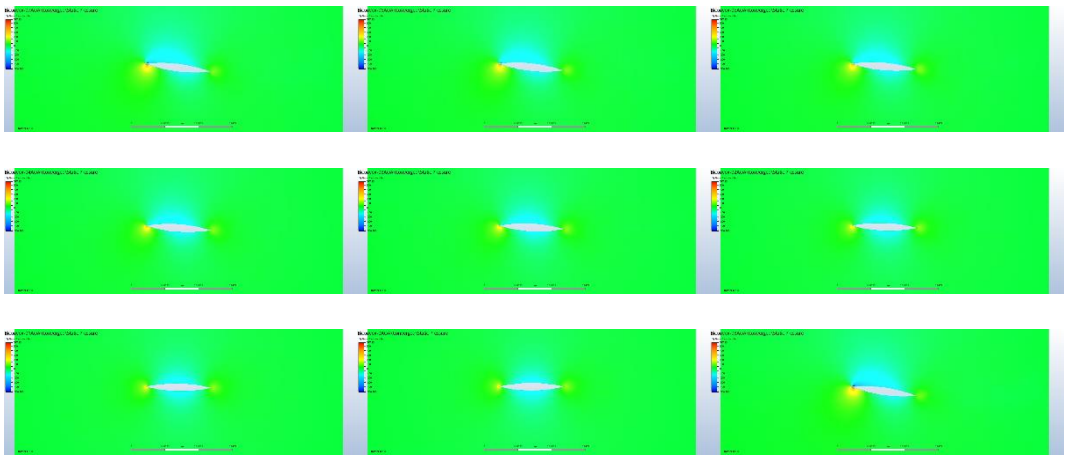

Figure 44: Pressure Field for a Biconvex Airfoil from Zero to Eight Angle of Attack.

RESULTS AND DISCUSSION

In this section we will discuss the leading-edge suction effect on wings comparing Autodesk CFD software, VORLAX [4], and the wing tunnel test data to simulate flow field around NACA 4-digit and biconvex airfoil and compare their aerodynamics features.

A. Verify CFD Results with Wind Tunnel Data and VORLAX Code

First, the reliability of the CFD should be tested. We can use the VORLAX code, inviscid data set, and wind tunnel data, viscous data set, as another benchmark to verify the convergence of the result from CFD software.

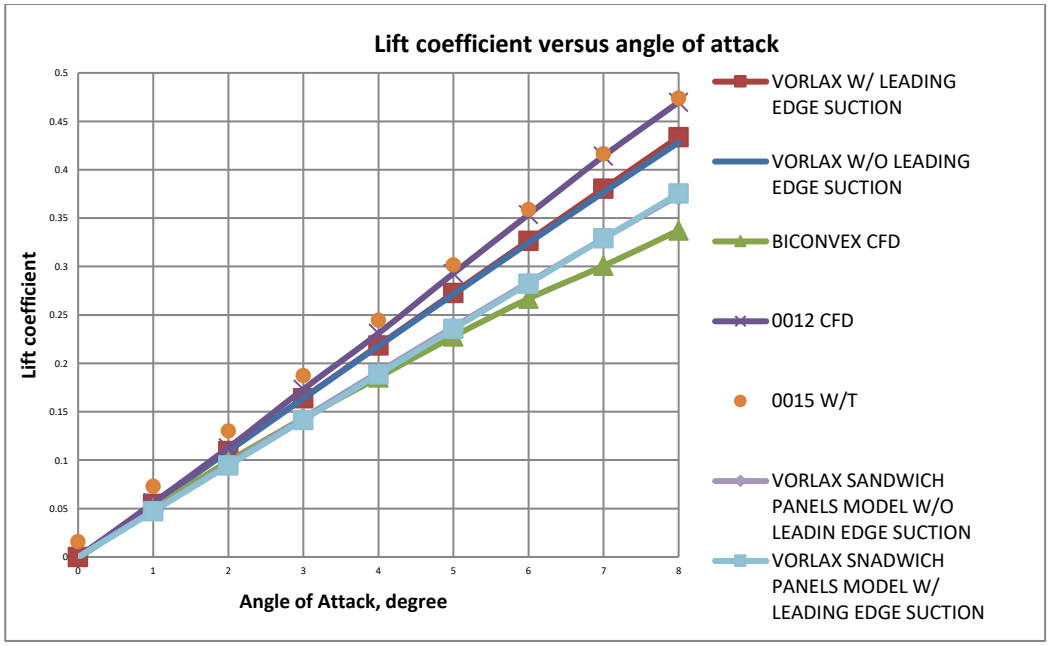

Figure 45: Lift Coefficient versus Angle of Attack

The plot shows the CL versus alpha from VORLAX code, CFD results, and wing tunnel results.

The lift coefficient is not a function of thickness; hence we can use NACA 0015 wind tunnel data to check NACA 0012 computational result; both models were run at a chord Reynolds number of ~200,000.

Refer to Figure 45. We can see the match is good between CFD, VORLAX, and Wind Tunnel Test for the 4-digit airfoils when comparing lift vs angle of attack.

Refer to drag polar in Figure 46, we can see that VORLAX models cannot predict the drag due to lift of the NACA 4-digit airfoils unless we use 100% of the analytical leading-edge suction correction. Similarly, to match the Biconvex solution, we need to apply 30% of the analytical leading-edge suction which the process of deciding how many percentages of the analytical leading-edge suction we need to apply to flat panel model shows in “Description of Flat Plate VORLAX Model”. In the absence of such a correction, the predicted drag due to lift (due merely to the rotation of the normal force vector) is too high to present the overall force in the axial direction for a biconvex wing loyally.

Thus, leading-edge suction must be considered. This form of suction can’t neglect the negative axial “pressure drag” contribution of thickness, which we can see the most of theories in previous section neglect the thickness effect so as the leading-edge suction term.

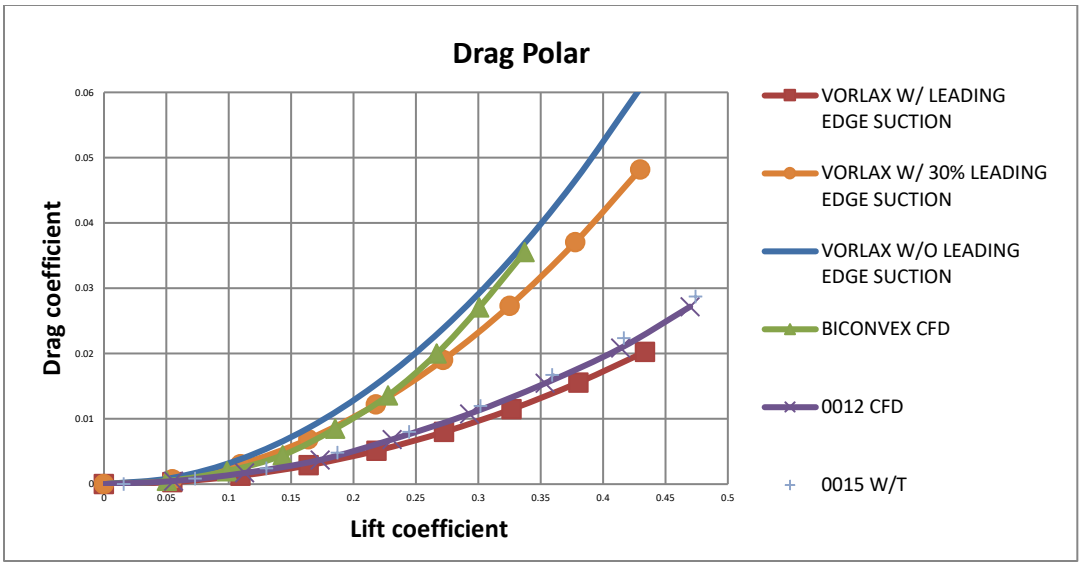

Figure 46: Drag Polar

The plot shows the CL versus CD from VORLAX code, CFD results, and wing tunnel results.

According to the limitation of the sandwich panels model for VORLAX code, we use the thin plate model data set for drag polar plot in Figure 46. Utilizing the method to decide leading edge suction in "Description of Flat Plate VORLAX Model" section can draw out the orange line which is more accurate to present the aerodynamic feature for a biconvex wing.

The CFD data set matches the wind tunnel result for NACA0015 and the thin flat plate model for VORLAX code. In the biconvex airfoil case, the CFD result has a little deflection for the last three data points. Based on the convergence test in CFD result, we can know the inaccuracy is from the difficulty of convergence with a high angle of attack. Overall, the CFD result is good enough to use as a viscous data set.

B. Utilize Pressure Loop to Observe the Leading-edge Suction.

Pressure loop plots are a classic British convention [16], [34] that shows the leading-edge suction force and its impact drag force by plotting pressure coefficient versus *z*-axis which is perpendicular to the wind axis.

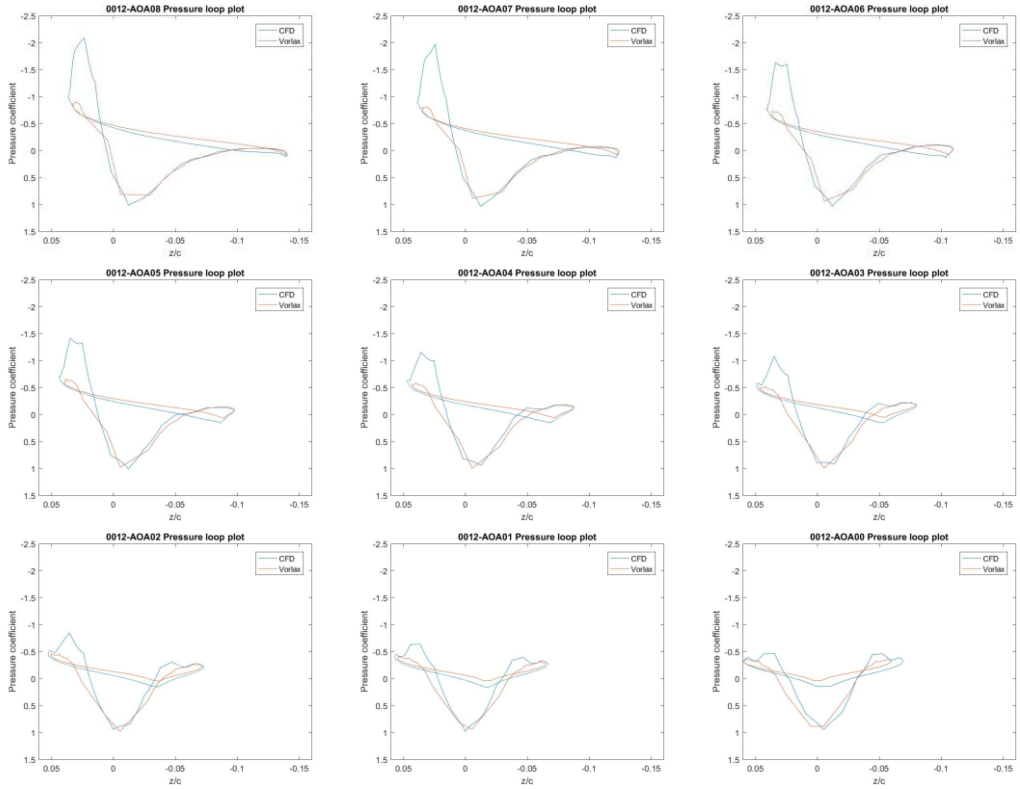

Figure 47: Pressure Loops for NACA 0012 Airfoil from 1° to 8° angle-of-attack

These plots show the pressure loop generated from both CFD software and VORLAX sandwich panels code for a NACA 0012 airfoil.

In the pressure loop plot, we can clearly visualize the different pressures in each position of the wing axis. If the pressure value is negative, it produces suction forces to pull the airfoil forward. On the contrary, the positive pressure is drag force resisting the

forward force. Moreover, the area surrounded by the curve indicates the total suction force if the area is in negative region or drag force if the area is in positive region.

By comparing with the red line generated from VORLAX without leading-edge suction result in Figure 47, we can see the trend is similar aside from the left enclosed region. Therefore, it is consistent with the fact that pure VORLAX result without the leading-edge multiplier[4] with almost no leading-edge suction, and the trend also shows the CFD simulation is good enough for analysis. With the same concept, the left region enclosed by blue line generated from CFD data grows as the angle-of-attack goes up, so the total leading-edge suction increases.

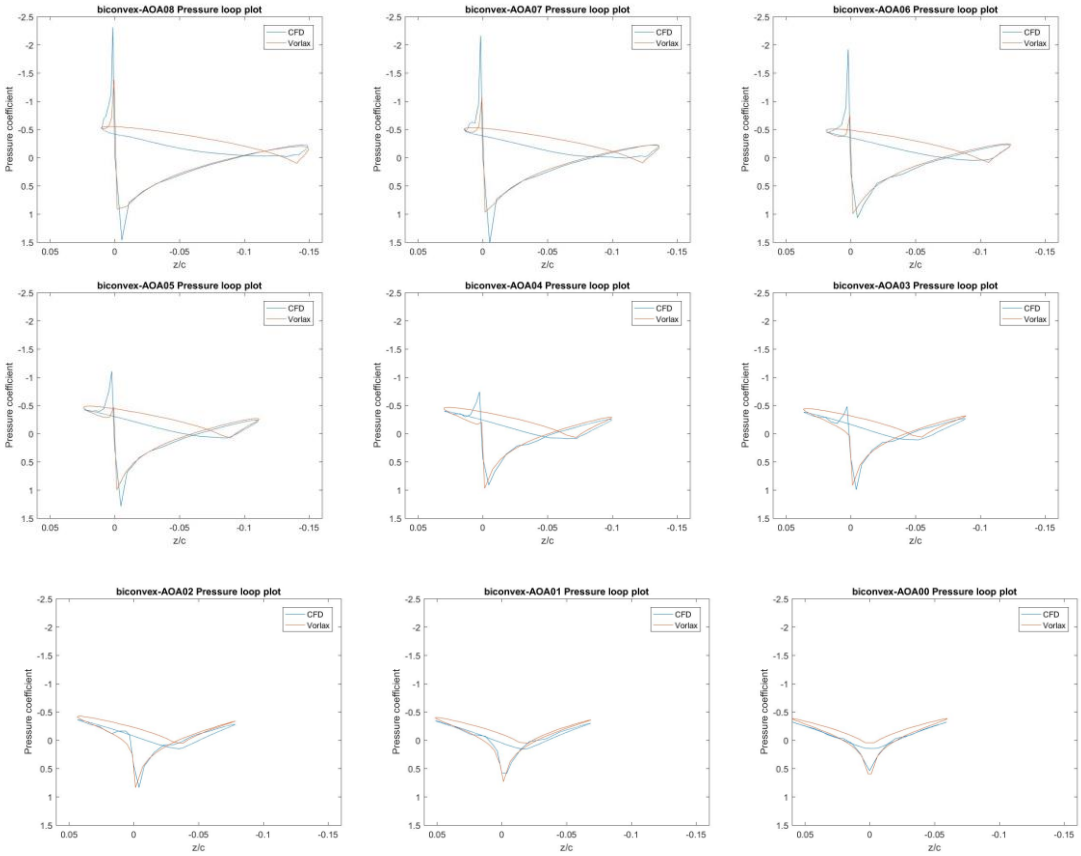

Figure 48: Pressure Loops for Biconvex Airfoil from One to Eight Angle-of-Attack

These plots show the pressure loops generate from both CFD software and VORLAX sandwich panels code for biconvex airfoil.

On the contrary, the sharp leading-edge cases in Figure 48 have different form of pressure loop plots. Comparing to the NACA 0012 airfoil, the biconvex airfoil has almost no suction force produced for both CFD and VORLAX data sets. Even looking at the highest angle of attack case, the area of suction force remains smaller than the blunt leading-edge airfoil. It shows that the same airfoil with identical chord length, thickness, and camber can generate extremely different aerodynamics features because of the difference of the leading-edge. In sum, leading-edge will affect the production of leading-edge suction.

C. Infer the Transverse Span Load to Extract the Classical Bound Vorticity Distribution

Span Loads is an important feature to present the three-dimensional effect of a wing. The lift coefficient versus span is a common setup for a span loads plot. However, Since VORLAX code only can generate spanwise normal force coefficient rather than spanwise lift coefficient, we compare VORLAX's Cn with CFD's Cn. According to the geometrical relationship between lift, drag, normal force, and axial force, we can formulate the equation as:

$$N = L\cos(\alpha) + D\sin(\alpha) \tag{96}$$

$$A = -L\sin(\alpha) + D\cos(\alpha) \tag{97}$$

$$L = N\cos(\alpha) - A\sin(\alpha) \tag{98}$$

$$D = N\sin(\alpha) + A\cos(\alpha) \tag{99}$$

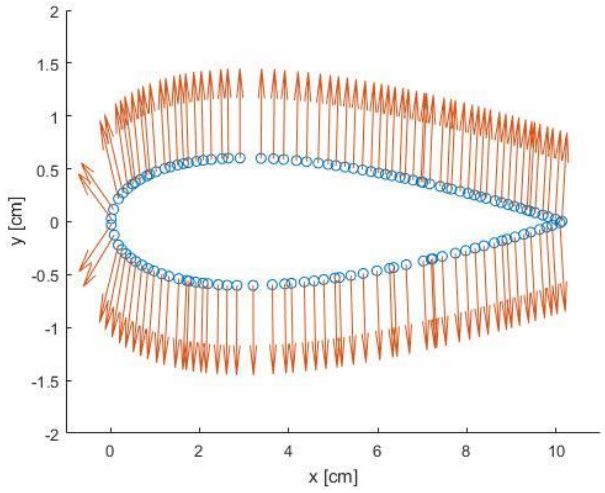

Figure 49: Normal Vector for the Middle Point of Each Panel.

The plot demonstrates the normal vector of part of mesh panels using for CFD software. The reverse direction is the vector of pressure force.

Because of small angle approximation, most of the theories we mention before assuming the normal force coefficient span loads will be identical with the lift coefficient span loads. In fact, the normal force can't use small approximation to assume that the sine component of the pressure acting on the panels are always zero and that the cosine component of the pressure acting on the panels are always one because the angles of the surfaces are not small enough to be suitable for small angle approximation especially at the region of leading-edge.

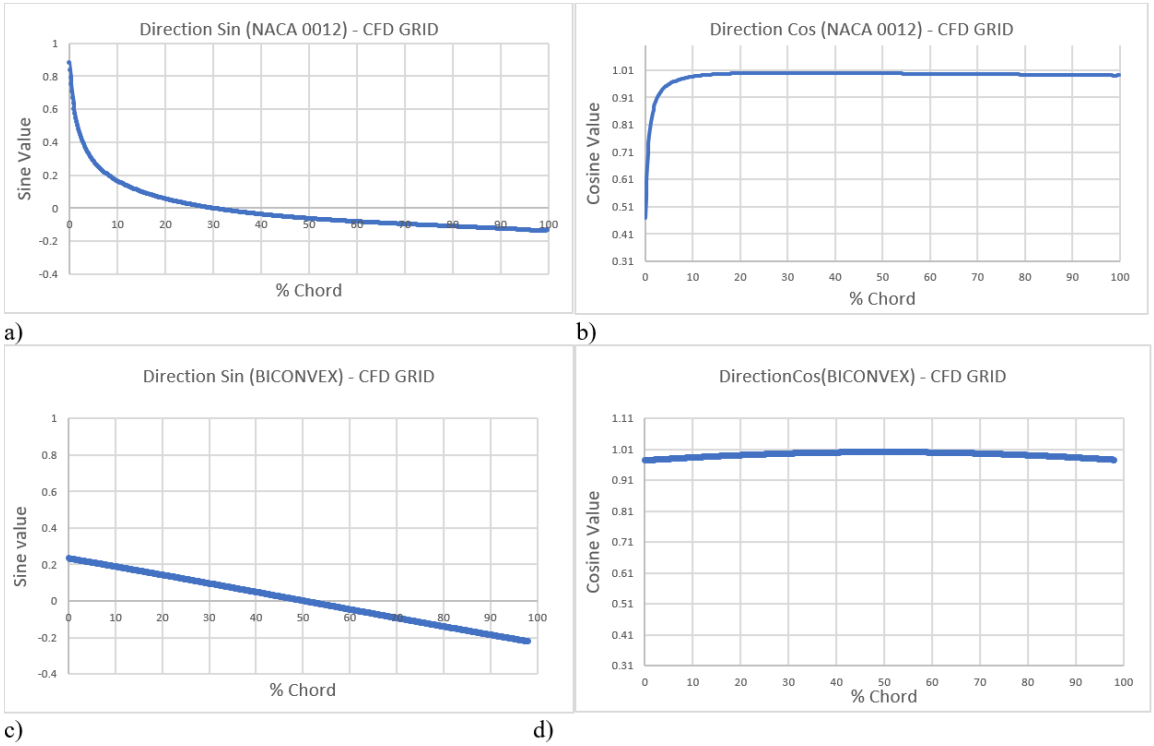

Figure 50: Comparison of Cosine and Sine Components for the Normal Cector of the Mesh Panels Between a NACA 0012 Airfoil and a Biconvex Airfoil.

These four plots show the cosine and sine components on each mesh panel generate by CFD software. Figure a and b are for a NACA 0012 airfoil. Figure c and d are for a biconvex airfoil.

The direction of the pressure force is perpendicular to the surfaces. In other words, the vector of pressure work on each mesh panel is paralleled to the normal direction of each panel. In Figure 49, it shows the normal vector on the surfaces of a NACA 0012 airfoil and we can see the arrows have more horizontal component when it approaches the leading-edge. The decomposition of the sine and cosine components, which is the direction of axial force and normal force, is demonstrated in Figure 50. To calculate the normal force coefficient Cn, the cosine component is the critical term for applying pressure force in the direction normal to the chord axis. The blunt leading-edge case in Figure 50a and Figure 50b indicate the pressure force in leading edge is applied to axial force mostly, which we know that is source of leading-edge suction. On the contrary, sharp leading-edge in Figure 6c and 6d don't have much pressure force transform to leading-edge suction. If we didn't calculate the cosine and sine component for each panel, the error is around 7% to 8% for a NACA 0012 airfoil and 5% to 6% for a biconvex airfoil.

Based on the method we use, the comparison of spanwise Cn distribution can be drawn correctly. Figure 51 indicates that the two results show the same trend no matter what the angle-of-attack is it. Aside from some fluctuations, the two curves have the same curvature. Since the VORLAX code simulates an inviscid flow, so we can know the viscous effect puts no influence on span loads. The comparison of NACA 0012 and biconvex airfoil in Figure 52 reveals a fact that leading edge will change the shape of span loads. Therefore, based on the two facts: the viscous effect won't change the span loads and the shape of span loads for NACA 0012 and a biconvex airfoil are not identical, we can say that the difference of blunt and sharp leading edge is caused by the inviscid effect.

In “Configuration Aerodynamics”, Mason mentions [35] a wing in inviscid flow generates drag and the drag is due to the effective angle-of-attack. In other words, the induced drag effect affects the shape of span loads, and we can say the shape of the leading edge might create different induced drag so that the shape of span loads changes.

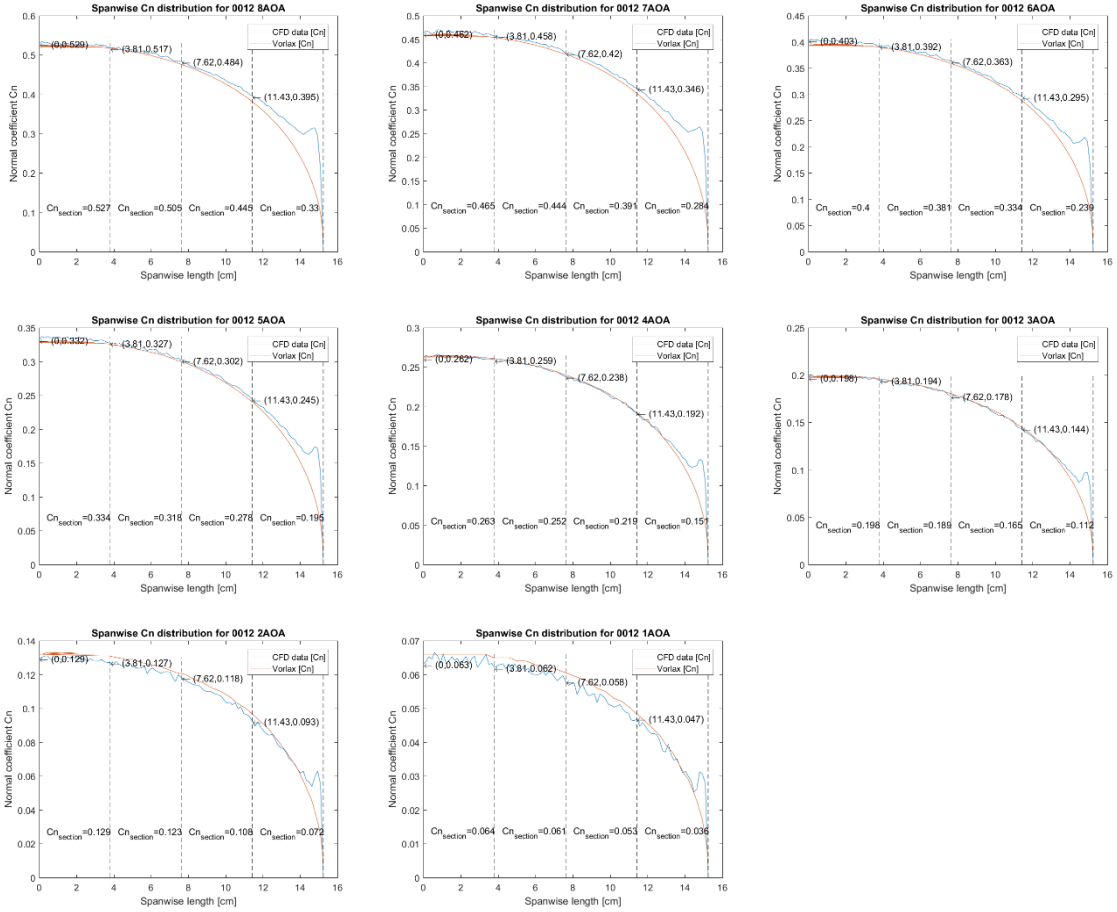

Figure 51: Span Loads for a NACA0012 Airfoil from One to Eight Angle of Attack.

These plots show the span loads calculated from CFD and VORLAX thin flat plate code for a NACA 0012 airfoil. The $Cn_{section}$ are the average of the normal force coefficient for each span section: centerline to ¼ span, ¼ span to ½ span, ½ span to ¾ span, and ¾ span to full span.

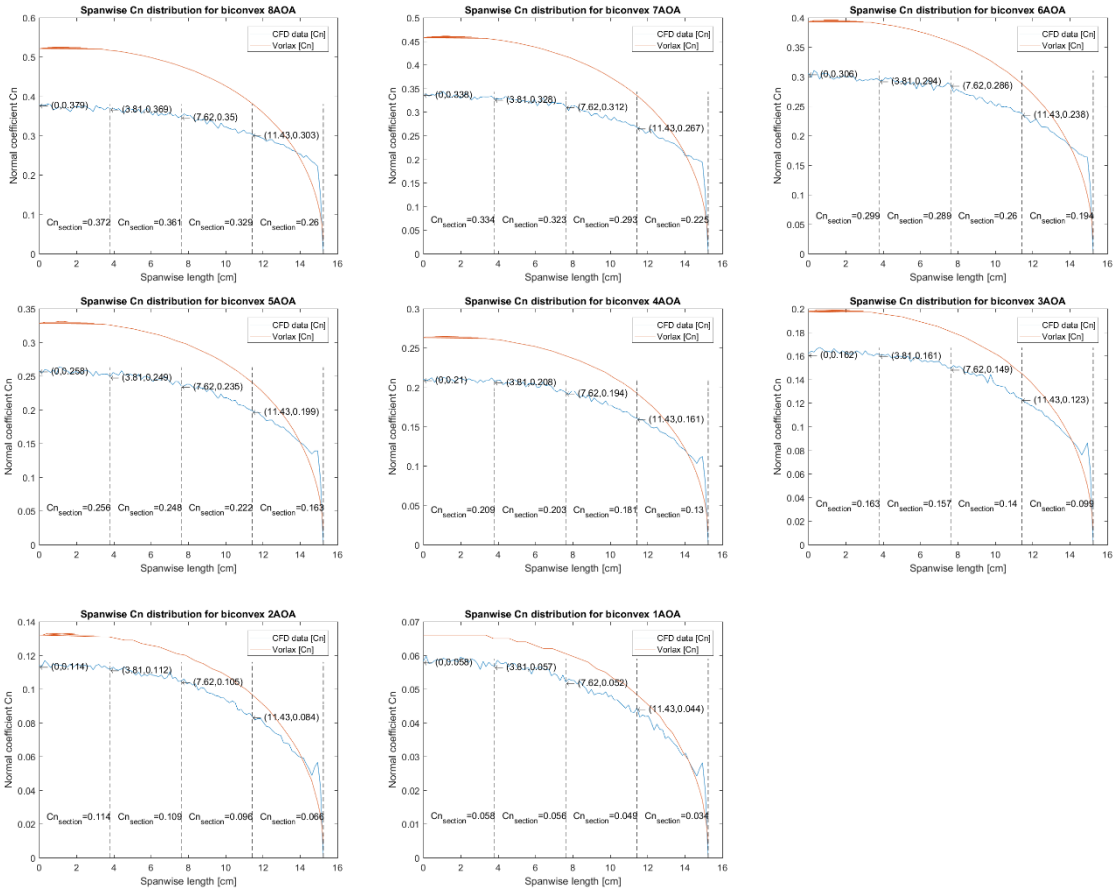

Figure 52: Span Loads for a Biconvex Airfoil from One to Eight Angle of Attack.

These plots show the span loads calculated from CFD and VORLAX code for a biconvex airfoil. The $Cn_{section}$ are the average of the normal force coefficient for each span section: centerline to ¼ span, ¼ span to ½ span, ½ span to ¾ span, and ¾ span to full span.

D. Chordwise Pressure Distribution

The chordwise pressure distribution is shown by pressure coefficient versus chord. A common approximation is to consider the area enclosed by the upper surface pressure distribution and lower surface pressure as the lift coefficient. Based on the concept we discussed in the previous section (Figure 50), we know the lift is not merely the upper surface pressure minus lower surface pressure like a flat plate airfoil since the pressure is normal to the surface instead of being perpendicular to the chord. Therefore, the approximation is not accurate when we analyze a thick airfoil or the one with a camber.

To get the correct force acting in the normal direction, the normal vector of each angle is essential to find the correct value of normal component like we did in span loads section. However, although traditional pressure distribution cannot derive the lift of a wing as we always believe before, it still a useful tool to demonstrate how different the pressure between the upper surface and lower surface area.

Figure 53 and Figure 54 are the pressure distribution plots for the blunt leading-edge model, NACA 0012 airfoil, and sharp leading-edge model, biconvex airfoil generated by CFD. For a biconvex airfoil in Figure 54, it shows that Cp decreases rapidly after the peak. A sharp leading-edge can face incoming flow with small front cross-section so that the velocity on the tip of the leading edge is higher and the absolute value of Cp can be larger, but the increasing front cross-section makes the velocity decade continuously. Therefore, the pressure difference between the upper surface and lower surface shrinks

very fast. On the contrary, although the flow hits the blunt leading-edge with a larger thickness in the front of the airfoil so that the pressure peak is not as high as the sharp leading-edge, blunt leading-edge has a shorter region for decreasing velocity and longer region to increase the flow speed or delay the flow speed reduction. Consequently, the pressure difference declines slower and the area enclosed by the curve is larger.

The VORLAX model, with its coarse grid, doesn't resolve the leading-edge suction "spike" as clearly as the CFD model. Thus, the axial forces integrated from VORLAX will differ.

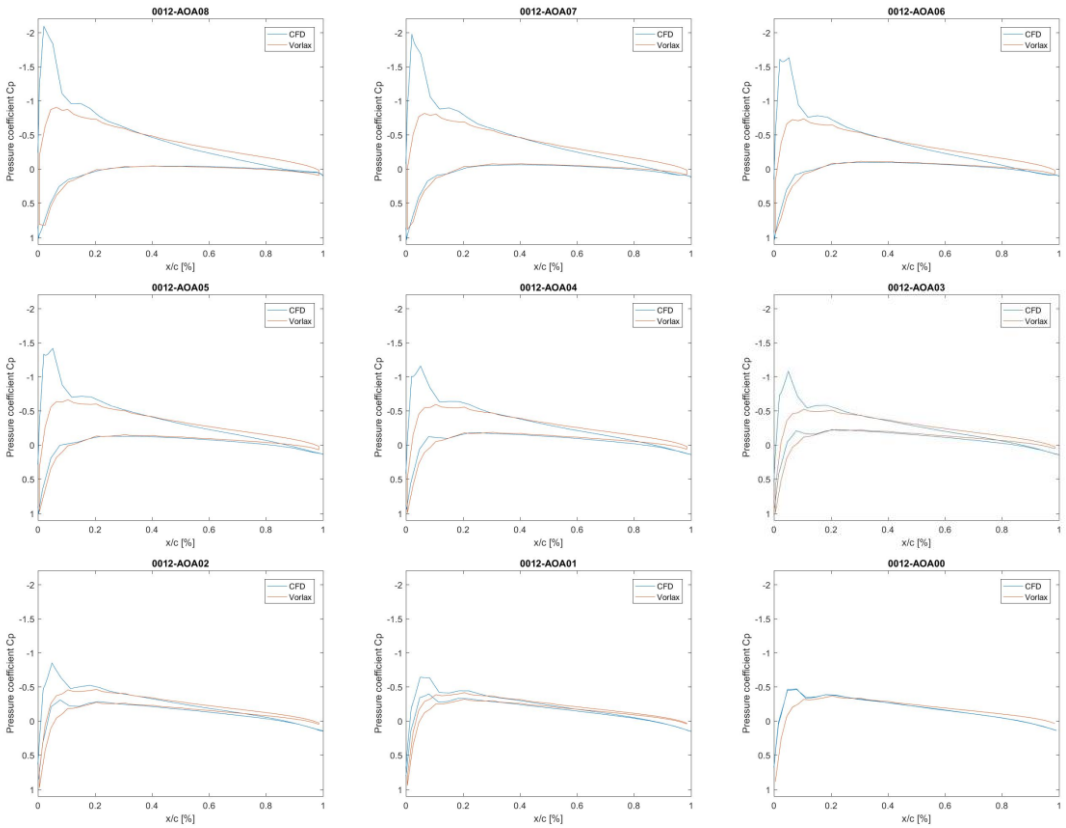

Figure 53: Pressure Distribution for a NACA 0012 Airfoil

These plots show the pressure distribution from zero angle-of-attack to eight angle-of-attack.

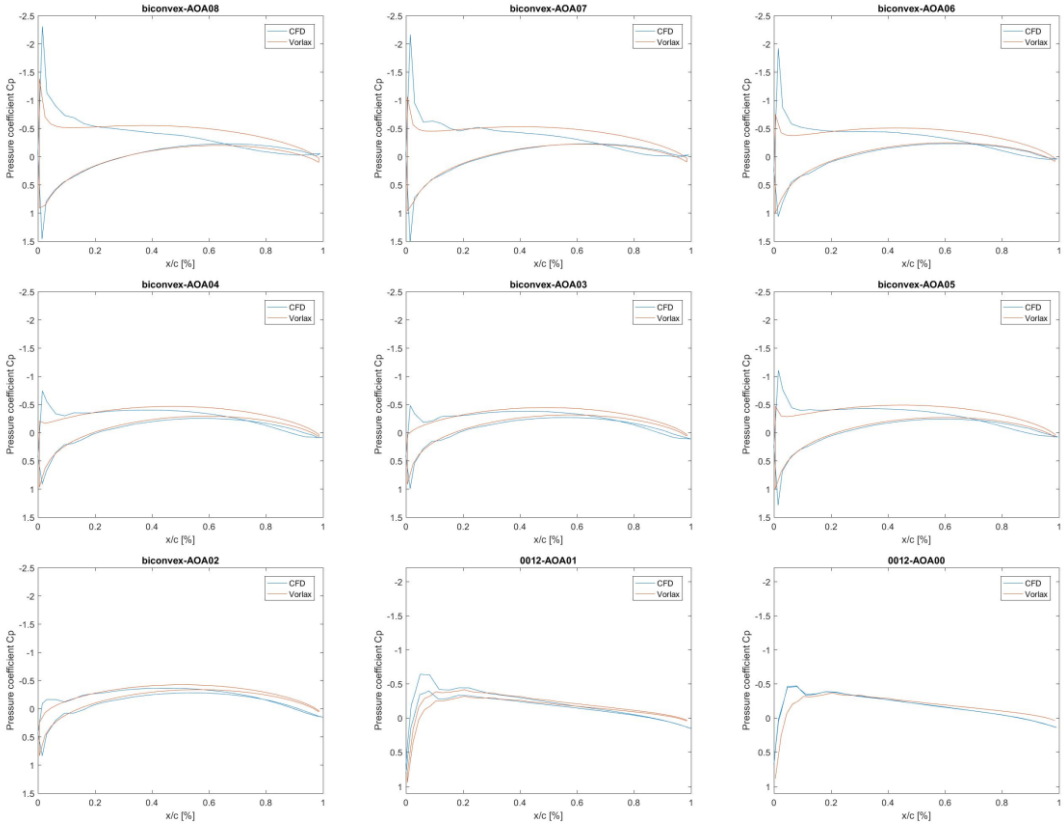

Figure 54: Pressure Distribution for a Biconvex 0012 Airfoil

These plots show the pressure distribution of a biconvex airfoil from zero angle-of-attack to eight angle-of-attack.

E. Mclean's Equation Verification

In Mclean's "Understanding Aerodynamics"[3], he derives a general formula from far-field momentum balance for induced drag.

$$D_i = \iint_{S_1} \frac{1}{2}\rho\left(-u_{1_i}^2 + v_{1_i}^2 + w_{1_i}^2\right)dS_1 \tag{47}$$

However, as we know, a different leading-edge will change the span loads from the previous section. We wonder whether this equation can present a correct result for two different leading-edge.

For the CFD result, we can use *TECPLOT* to integrate the u, v, w velocities across the entire plane we want.

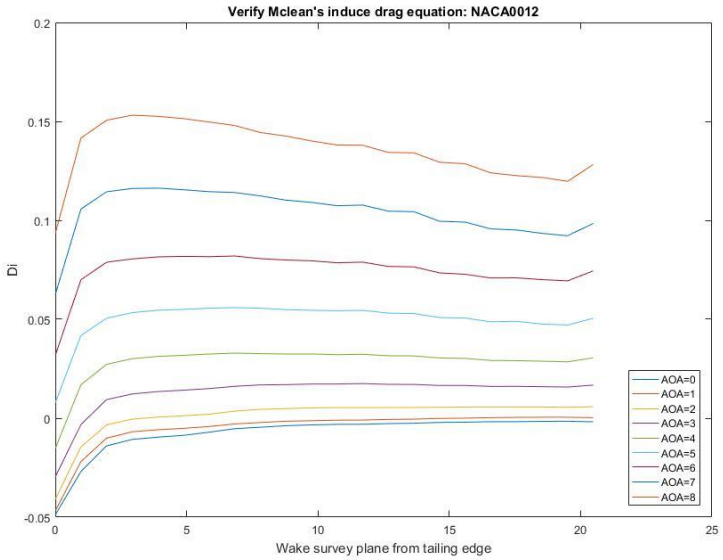

Figure 55: Wake Survey Plane and Induced Drag for a NACA0012 Airfoil from Mclean's Equation

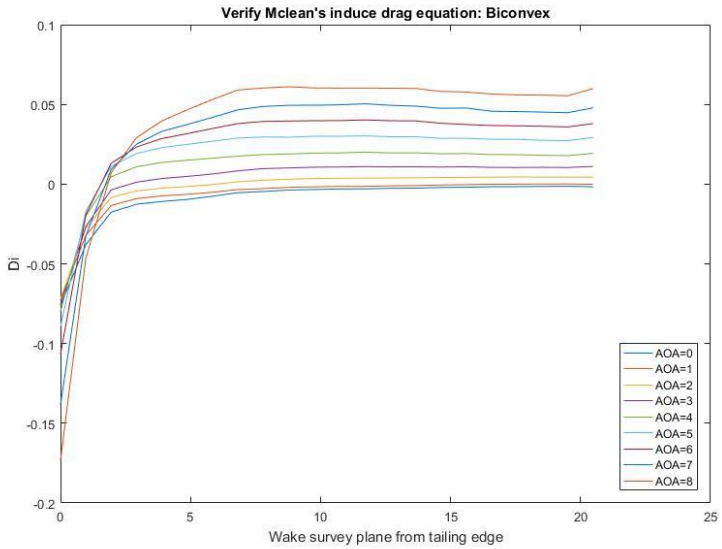

Figure 56: Wake Survey Plane and Induced Drag for a Biconvex Airfoil from Mclean's Equation

The choice of distance can take Brune's paper [36] as a reference. In this paper, he states the lift and induced drag are roughly independent from the location of the wake survey location we choose. Technically, we can choose any distance away from trailing-edge because we don't have limited measuring points as the experiment does. However, to eliminate the effect from tailing edge and wall because of the imperfection of convergence, the selection of wake survey plane needs to be as close as possible to the trailing edge, but it won't be affected by trailing-edge flow. With 20 different planes in Figure 55, Figure 56, we can see the continuous change of the drag value as the increase of distance away from the trailing edge. This work helps us to decide where is far enough to take as the survey plane.

Another data set is from VORLAX examination. The data set is made in body axis, which if we what to apply the Mclean's equation, either a transformation from body axis to wind axis or subtraction from mean downwash is needed. In Figure 57 and Figure 58, we can see there is no much different if we utilize either methods or combining both.

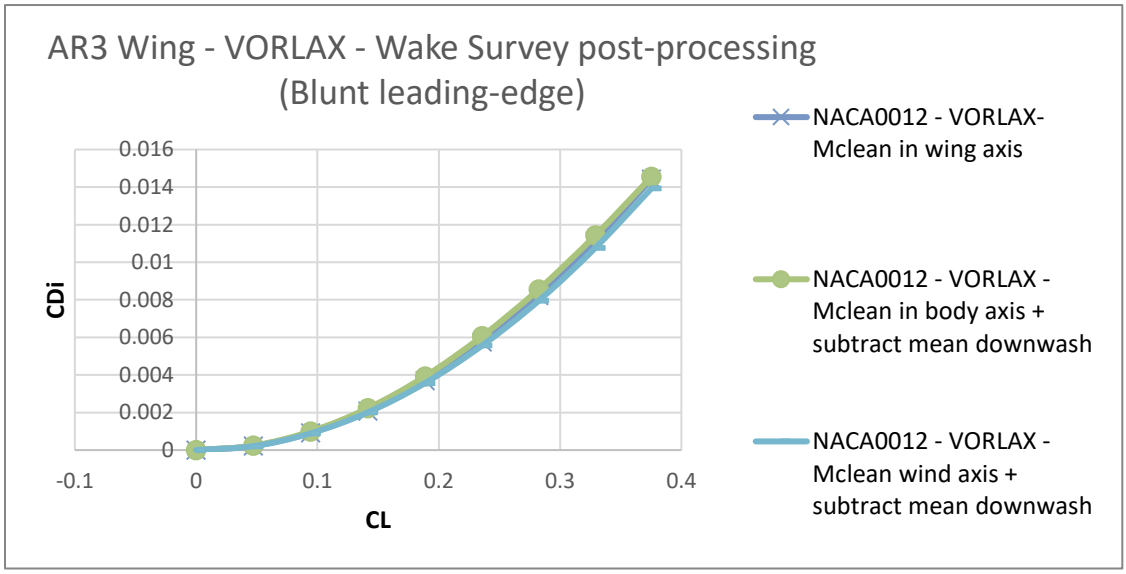

Figure 57: Post-processing for VORLAX Wake Integration (Blunt leading-edge)

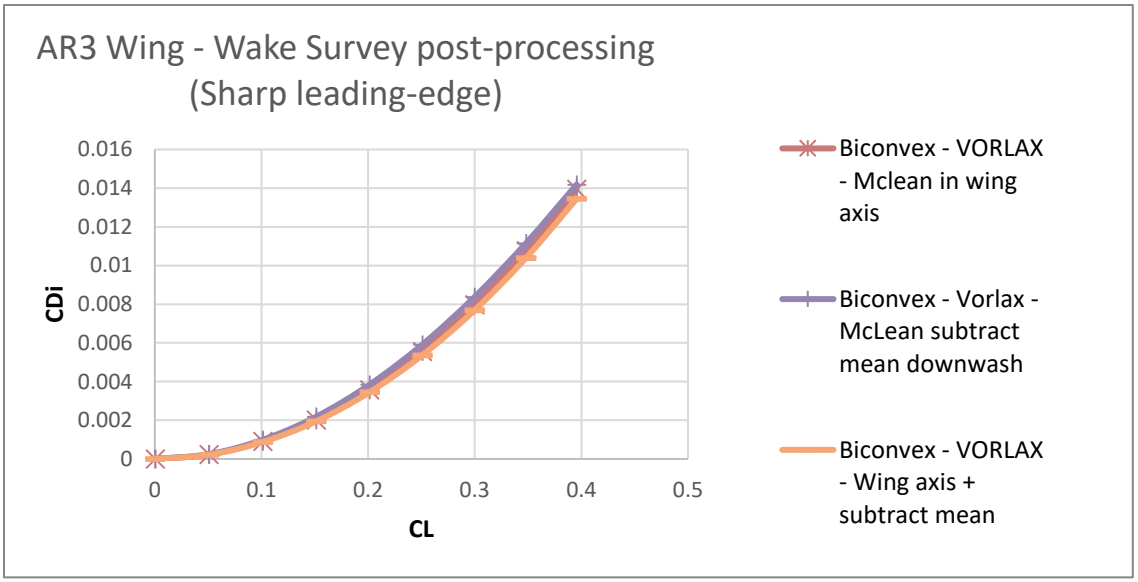

Figure 58: Post-processing for VORLAX Wake Integration (Sharp leading-edge)

Therefore, we take the result after applying transformation and subtraction of the mean downwash as the VORLAX's wake integral data and combine it with CFD's wake integral data. As we know from the famous decomposition of drag:

$$\mathrm{C_D} = \mathrm{C_{D_i}} + C_{D_0} \tag{100}$$

The induced drag can simply be calculated by $\mathrm{C_D} - C_{D_0}$, where $\mathrm{C_{D_0}}$ is the drag when the angle of attack is zero. It looks reasonable, but the viscous drag term also increases when the angle of attack becomes higher. In order to present a proper induced drag value for comparison, the equation can be rewritten as:

$$\mathrm{C_{D_i}} = C_D - C_{D_p} - C_{D_0} \tag{101}$$

Where pressure drag coefficient C_{D_p} can be derived from the pressure different between inlet and outlet of the control volume.

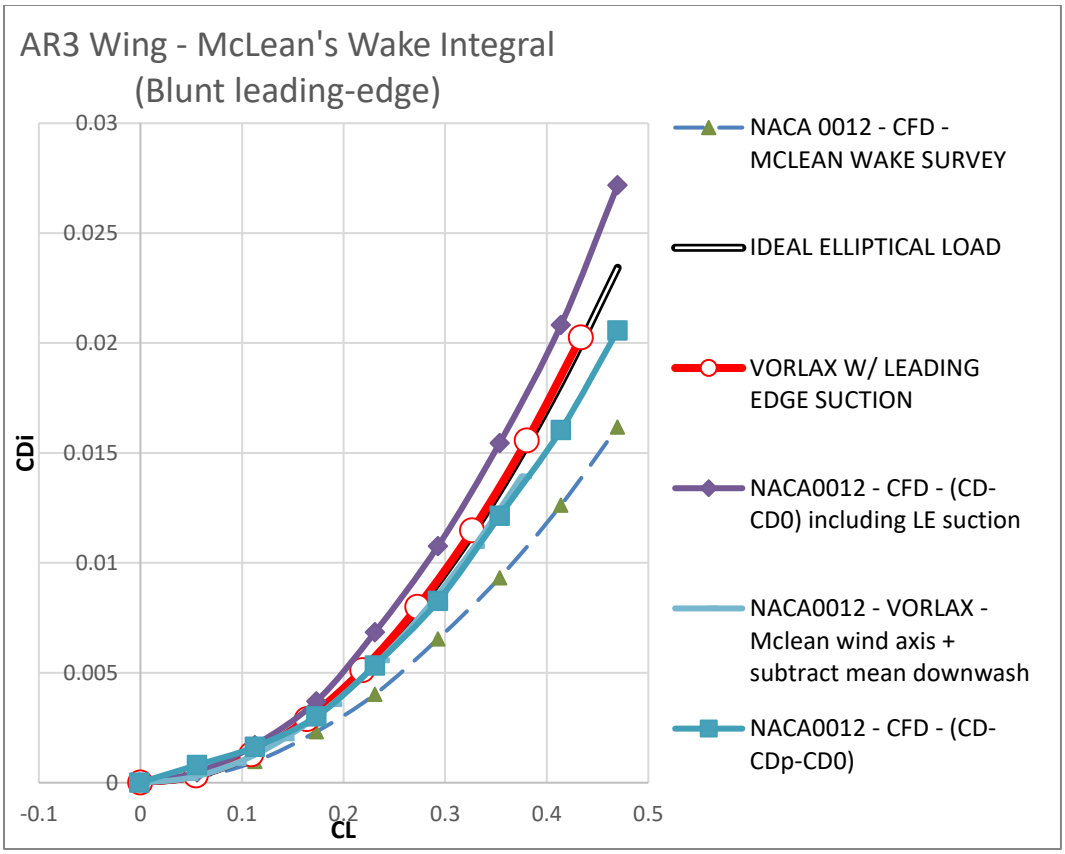

Figure 59: Mclean's Wake Integral for Blunt Leading-edge

In Figure 34, the VORLAX's result seems to match the Mclean's equation. CFD result is closed to the line, but it didn't fit as good as VORLAX. The difference between VORLAX and CFD is around 10%-20% which we can treat as the influence of viscous effect. However, the sharp leading edge in Figure 35 shows something interesting. Not only the CFD's result but also the VORLAX's result has a huge gap between the induced drag and Mclean's answer. Besides, we can see the induced drag from three different models (VORLAX sandwich panels, VORLAX flat panels, and CFD three-dimensional model) are pretty similar to each other. From here, the model shows the inaccuracy of Mclean's prediction does not originate from any viscous effect. Another important fact is

that Mclean's result for both cases are the same which means the two airfoils have the same wake flow.

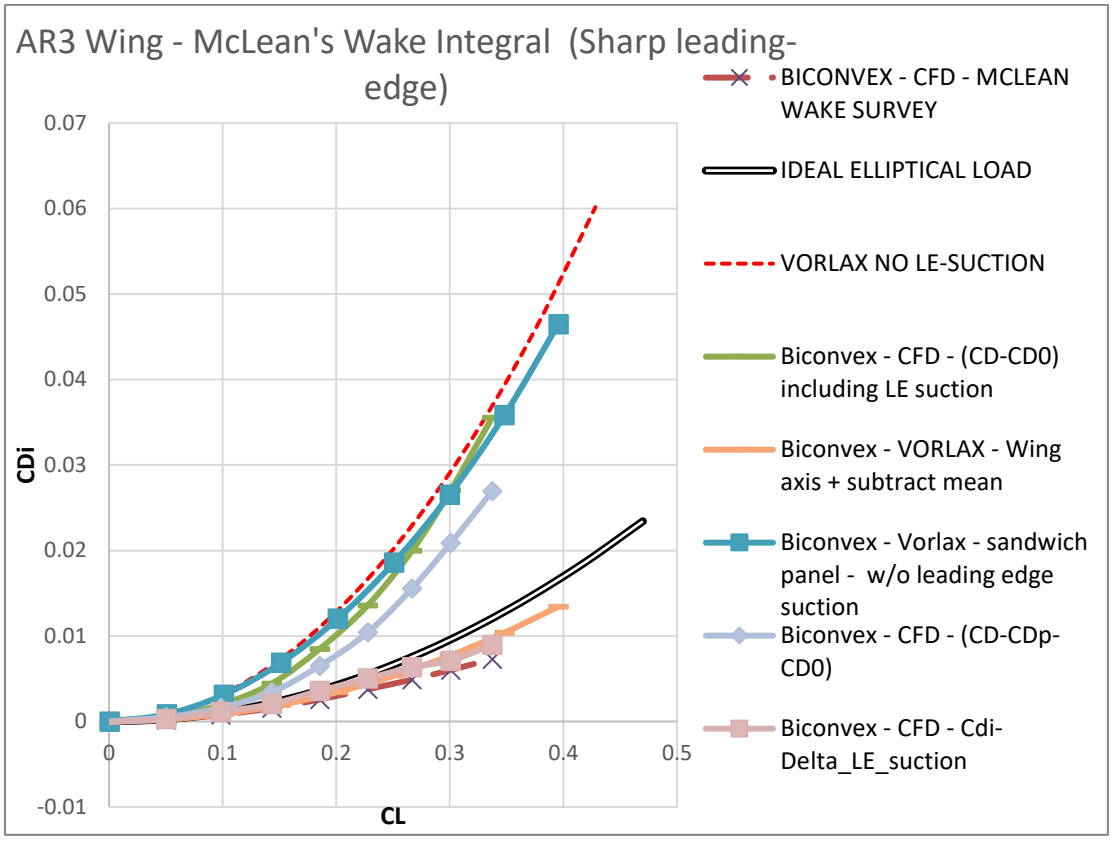

Figure 60: Mclean's Wake Integral for Sharp Leading-edge

Let's recall the fact that CFD captures viscous effects, which VORLAX neglects. It means the difference is not because of the viscous effect. In geometry perspective, the two cases are almost identical except for the leading edge. Hence, we can guess that something must be happening in leading-edge. There are two assumptions may cause this phenomenon.

1. There are some vortexes generated before survey plane => wake survey can't collect the all energy loss.
2. Mclean's equation didn't consider the leading-edge suction term.

According to the first assumption, we should be able to see the difference of the flow field between blunt leading-edge and sharp leading-edge.

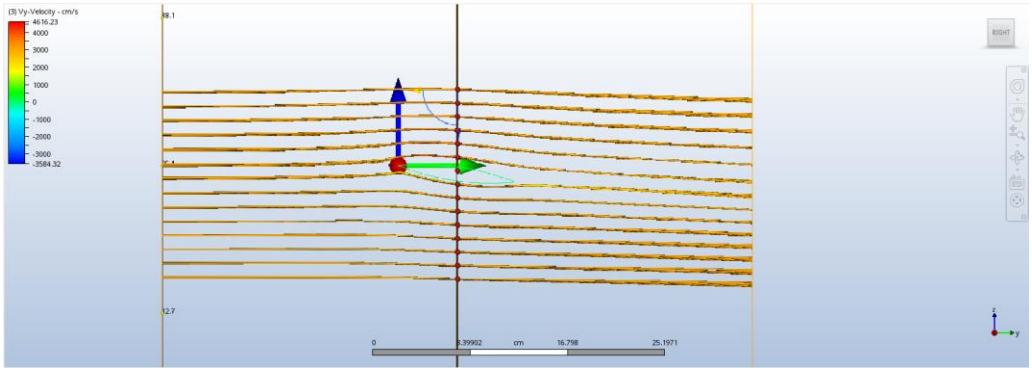

Figure 61: Velocity Flow Across a Biconvex Airfoil

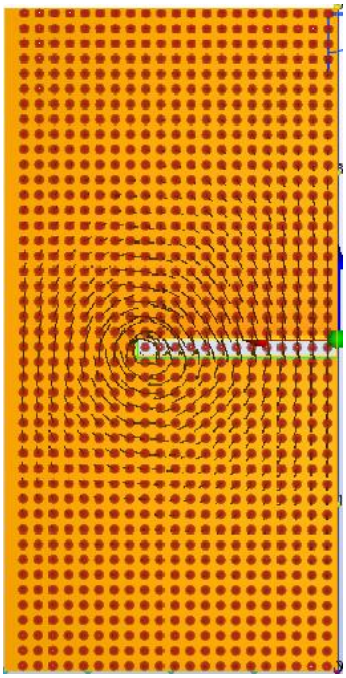

Figure 62: The Vortex Behind a Biconvex Airfoil

In Figure 61 and Figure 62, we can see a smooth flow across a biconvex airfoil and generated shed vortex near the tip. It proves the concept of wake integration is correct. If the concept is right, but the result only can apply to the blunt leading-edge case. It means the equation has a missing term. The second assumption can be tested by calculating the difference of leading-edge suction and then add it to sharp leading-edge, so it can simulate a biconvex airfoil with NACA0012 leading-edge suction.

Assume that Mclean's result can present the induced drag correctly without missing any term. Since the derived induced drag is higher than Mclean's result which we assume that is the real induced drag, the leading-edge thrust will be negative to match the situation.

However, we already proved that the biconvex has a small positive leading-edge suction in Figure 63.

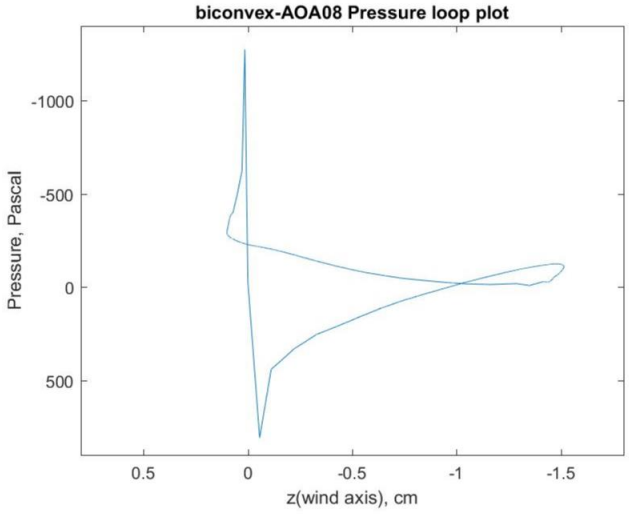

Figure 63: The Pressure Loop for a Biconvex Wing at 8° angle-of-attack. (CFD only)

Based on this, we are almost sure that Mclean's equation has something missing and the term is a function of angle of attack, which is second assumption.

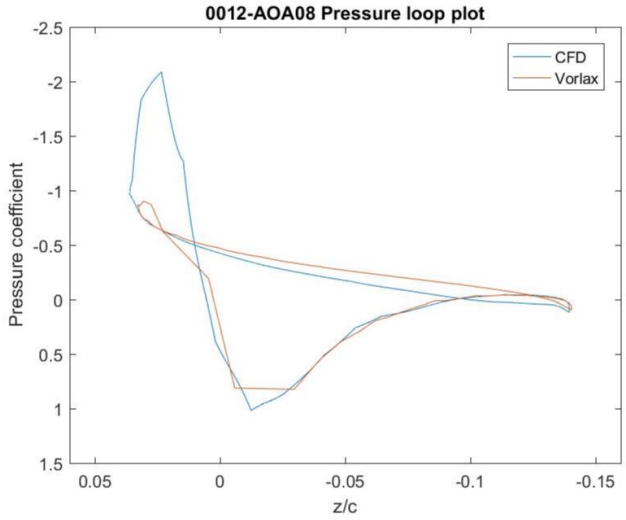

Figure 64: The Pressure Loop for a NACA0012 Wing at 8° angle-of-attack. (Both CFD and VORLAX)

According to the result so far, the leading-edge suction seems to be the only factor between the two airfoils which is possible to make the difference in value, and the blunt leading-edge result looks good in Figure 64. (Notes that the VORLAX result cannot capture the leading-edge suction.)

The way Mclean calculates the induced drag is to derive the energy losses in the wake, called wake survey. Based on Kelvin's circulation theorem, the energy of the shed

vortex is equal to the bound vortex and the bound vorticity is the one to generated lift to each panel. The lift also produces a forward and backward thrust which we called leading-edge suction. Therefore, blunt and sharp leading-edge have the same or similar lift for each panel, but because of the shape of leading-edge they distribute their lift (normal to each panels) to leading-edge suction with a different ratio (see Figure 65).

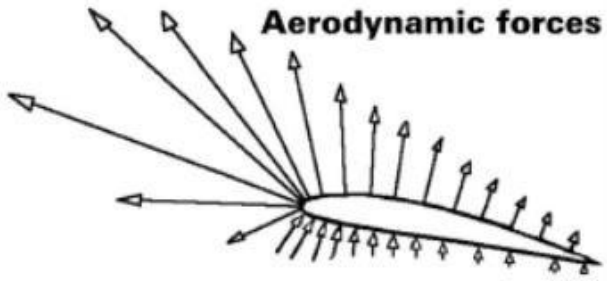

Figure 65: Pressure Force Distribution. [37]

We can see the wake survey in this perspective:

Wake Integration = the energy of shed vortex = the energy of bound vortex

= the sum of lift on each panel = normal vector of some panels is pointed to vertical direction, but some is points to horizontal direction.

= energy to generated lift (wing axis) + energy to generated leading-edge thrust.

= induced drag (+) + leading-edge suction (-).

Wake Integration == induced drag (+) + leading-edge suction (-).

Total drag = induced drag + leading-edge suction (-) + profile drag.

Total drag = Wake Integration - leading-edge suction (-) + profile drag

Total drag (C_D) – profile drag (C_{D_0}) = Wake survey - leading-edge suction (-)

$C_D - C_{D_0}$ = Mclean's result – LE_suction

If the Mclean's result for blunt and sharp leading-edge are the same or similar, then

$$\left(C_D - C_{D_0}\right)_{blunt} - \left(C_D - C_{D_0}\right)_{sharp} = (LE_{suction})_{sharp} - (LE_{suction})_{blunt}$$

Also, we know the Mclean's result is fairly close to blunt leading-edge result,

$\left(C_D - C_{D_0}\right)_{blunt}$ = Mclean's result.

$$\left(C_D - C_{D_0}\right)_{blunt} = \left(C_D - C_{D_0}\right)_{sharp} - (LE_{suction})_{sharp} + (LE_{suction})_{blunt}$$

Mclean's result = $\left(\mathrm{C_D} - C_{D_0}\right)_{sharp} - \Delta LE_{suction}$

Therefore, we can use the difference of leading edge thrust to correct the Mclean's equation in Figure 60.

In Figure 54, the "*CDi – delta_LEsuction*" turns out to fit the Mclean's result with reasonable accuracy. The result of correction is good when the angle-of-attack is small. The error for high angle of attack can be seen as the imperfect of CFD convergence. As we mentioned before, the difference does not originate from the viscous effect. We can also use the inviscid result to verify this theory again if the leading-edge suction term can be extracted from VORLAX. However, the method that VORLAX uses to simulate the thick airfoil is to use two vortex lattice layers where the joints are at the leading-edge and trailing-edge, so the assumption can't be verified by the data set we have. Now, we know that the missing term in Mclean's equation is the leading-edge suction term based on the result, but a question remains; why the differences of the leading-edge thrust can't be detected in the wake? In previous discussion, we note that the Mclean's equation accounts for the energy of wake, but the shed vorticity in the wake is not equal to the lift but bound vorticity, which is the pressure force on the surface. Moreover, the pressure force is the source of lift and leading-edge suction. Also, the Mclean's result of the blunt leading-edge wing can present the real situation properly. Therefore, the fact is that the Mclean's equation always assumes the wings have full leading-edge suction so it can't derive the induced drag for sharp leading-edge wings correctly.

CONCLUSION

For induced drag classic derivation, the theories discussed in the Prior Art section neglect thickness. They calculate the induced drag from a rotation of normal forces into the drag direction. The theories do not consider the curvature or thickness of the surface; thus, they claim pressure forces are always pointed orthogonal to the airfoil. That is also the reason why Kutta-Joukowski theorem can be written in such a concise from:

$L'^{(y_0)} = \rho_\infty V_\infty \Gamma(y_0)$# 8Where Γ is the circulation (see Figure 3) and y0 is a specific transverse "strip" on the span.

Classical methods assume all airfoils are transformed from perfect, inviscid flow around a cylinder. In this simplified model, the sum of pressure forces on the surface of a circle in the drag direction is zero. This property of ideal inviscid flow means that all follow-up theories developed from the Kutta-Joukowski theorem make the same assumption: the airfoils don't have thickness effects and cannot develop axial forces due to inviscid flow mechanisms.

However, we know that the common airfoils have sharp trailing edges. The Kutta condition and Kelvin's circulation theorem explain how the finite angle or cusp trailing edge can produce a starting vortex: The "vorticity" of this vortex is identical to the "bound vorticity" which is the circulation in the Kutta-Joukowski theorem.

Mclean emphasizes that induced drag is a measure of the shed vorticity in the wake. Based on the development of these theories, Mclean believes the energy loss in the wake goes back to the consequence of lift because of the energy conservation and Kelvin's theorem. His logic is correct, but we know the source of his theory is the Kutta-Joukowski theorem which assumes the airfoils have round leading-edge and sharp trailing-edge (with Kutta condition). In this perspective, Mclean's Wake Survey Method also neglects the thickness effect and presumes all airfoil have a blunt leading edge and sharp trailing edges. Thus, classical methods to derive induced drag apply to ideal blunt leading-edge airfoils only.

Viscous and inviscid test data also show the fact that a wake survey doesn't match with the value directly derived from the pressure force acting on the surface. The critical point is the leading-edge suction caused by the shape of the leading-edge. To be more specific, the classical theories do not consider the change of leading-edge suction along with the shape of the leading edge. Instead, they assume all airfoils have "full" leading-edge suction.

Polhamus is the first to provide the idea of leading-edge suction. Even his theory does not fully match with the lifting line theory: the concept of Polhamus's paper shows how to "correct" induced drag. The difference between Mclean's Wake Survey and real test data for a sharp leading-edge wing can be explained by the lack of a leading-edge suction term. Once the correct value is applied to the Mclean's result, the data becomes reasonably close. In conclusion, classical methods can only derive induced drag apply for ideal blunt leading-edge airfoils. We can correct the result by knowing the difference of

leading-edge suction between full leading-edge suction wings and partially leading-edge suction wings.

REFERENCES

[1] M. M. Munk, “Fundamentals of Fluid Dynamics for Aircraft Designers,” 1933.

[2] D. J. Dulin and T. T. Takahashi, “Design Implications of Elliptical Planform Wings,” *AIAA 2015-0397*, no. January, pp. 1–13, 2015.

[3] D. McLean, *Understanding aerodynamics : arguing from the real physics*. Wiley-Blackwell, 2013.

[4] L. R. Miranda, R. D. Elliot, and W. M. Baker, “A generalized vortex lattice method for subsonic and supersonic flow applications,” *NASA Contract. Rep. 2865*, 1977.

[5] M. Mahdi, “Prediction of Wing Downwash Using CFD,” *INCAS Bull.*, vol. 7, no. 2, pp. 105–111, 1975.

[6] E. Larrabee, “The aerodynamic design of sailplane tail assemblies,” *Tech. Soar.*, vol. 5, no. 1, pp. 21–28, 1976.

[7] D. Kuchemann, “Investigation of the lift distribution over the separate wings of a biplane,” *NASA Tech. Rep.*, no. 889, 1939.

[8] J. D. Anderson, *Fundamentals of Aerodynamics*, Fiith edit. Tata McGraw-Hill Education, 2010.

[9] R. M. Cummings, M. B. Giles, and G. N. Shrinivas, “Analysis of the elements of drag in three-dimensional viscous and inviscid flows,” *AIAA 96-2482*, pp. 1–15, Jun. 1996.

[10] M. Drela, *Flight Vehicle Aerodynamics*. MIT press, 2014.

[11] N. Joukowsky, “Über die Konturen der Tragflächen der Drachenflieger,” vol. 1, pp. 281–284, 1910.

[12] A. M. Kuethe and J. D. Schetzer, *Foundations of Aerodynamics*. 1959.

[13] T. Takahashi, “On the decomposition of drag components from wake flow measurements,” in *AIAA 97-0717*, 1997, pp. 1–10.

[14] W. Bollay, “Determination of Profile Drag from Measurements in the Wake a Body,” *J. Aeronaut. Sci.*, vol. 5, no. 6, pp. 245–248, Apr. 1938.

[15] A. Betz, “A method for the direct determination of wing-section drag,” *NACA TM-337*, 1925.

[16] L. Bairstow and B. Melvill Jones, “Experiments on models of aeroplane wings,” *ARC R&M*, no. 60, 1912.

[17] J. Schirra, “Accurate induced drag prediction for highly non-planar lifting

systems," pp. 61–62, 2016.

[18] S. C. Smith, "A computational and experimental study of nonlinear aspects of induced drag," *NASA Tech. Rep. 3598*, pp. 89–92, 1996.

[19] M. Dogar, "An Experimental Investigation of Aerodynamics and Flow Characteristics of Slender and Non-Slender Delta Wings," McGill University, 2012.

[20] F. L. A. Ganzevles, A. C. de Bruin, and W. Puffert-Meissner, "A Quantitative Analysis of Viscous and Lift-induced Drag Components from Detailed Wake Measurements behind a Half-Span Model," 2002.

[21] J. Katz and A. Plotkin, *Low-Speed Aerodynamics*. Cambridge university press, 2001.

[22] H. Garner, "Multhopp's subsonic lifting-surface theory of wings in slow pitching oscillations," *ARC R&M No. 2885*, 1956.

[23] H. Multhopp, "Methods for calculating the lift distribution of wings (subsonic lifting-surface theory)," *ARC R&M No. 2884*, 1955.

[24] J. Bertin and R. Cummings, *Aerodynamics for Engineers*. Prentice Hall, NJ, 2002.

[25] W. P. Henderson, "Effects of wing leading-edge radius and Reynolds number on longitudinal aerodynamic characteristics of highly swept wing-body configurations at subsonic speeds," *NASA TN D-8361*, 1976.

[26] E. C. Polhamus, "A concept of the vortex lift of sharp-edge delta wings based on a leading-edge-suction analogy," 1966.

[27] H. W. Carlson, R. J. Mack, and R. L. Barger, "Estimation of attainable leading-edge thrust for wings at subsonic and supersonic speeds," *NASA TP 1500*, 1979.

[28] J. J. Kirkman and T. T. Takahashi, "Revisiting the Transonic Similarity Rule: Critical Mach Number Prediction Using Potential Flow Solutions," *AIAA 2016-4329*, pp. 1–20, 2015.

[29] J. Lamar and R. Margason, "Vortex-lattice FORTRAN program for estimating subsonic aerodynamic characteristics of complex planforms," *NASA TN D-6142*, p. 20, 1971.

[30] D. Cohen and R. T. Jones, *High speed wing theory*. Princeton University Press, 1960.

[31] M. Morrow, "Leading Edge Geometry Effects on Pressure Drag and Pressure Thrust for Various Wing Geometries," 2017.

[32] G. P. Kingsley, "Wind Tunnel Test Data of an Untapered Aspect Ratio 4 0015 Wing, Unpublished Raw Data," 2018.

[33] “Turbulent model for Autodesk CFD,” 2016. [Online]. Available: http://www.autodesk.com/products/cfd/features/all/list-view.

[34] H. Pearcey, “The aerodynamic design of section shapes for swept wings,” *Adv. Aeronaut. Sci.*, vol. 3, pp. 277–322, 1962.

[35] W. H. Mason, “Configuration aerodynamics,” *Virginia Tech*, pp. 3–41, 2006.

[36] G. W. Brune and P. W. Bogataj, “Induced drag of a simple wing from wake measurements,” *SAE Tech. Pap. 901934*, pp. 1889–1901, 1990.

[37] P. Falsehood, “Physical principles of winged flight,” 2009. [Online]. Available: http://regenpress.com.